Nonlinear optical characterization of LiNbO₃.
I. Theoretical analysis of
Maker fringe patterns for *x*-cut wafers

N. A. Sanford and J. A. Aust

National Institute of Standards and Technology, Optoelectronics Division 815,
325 Broadway, Boulder, Colorado 80303

Maker fringe analysis was adapted to *x*-cut LiNbO₃ wafers to examine variations in birefringence, thickness, and photoelastic strain.   The pump beam was polarized parallel to the crystalline *y* axis and produced *e*- and *o*-polarized Maker fringes, owing to d_{31} and d_{22}, respectively, by rotation of the sample about the *y* axis.   Fitting our model to the *o*-polarized data enabled computation of the sample thickness to an uncertainty of approximately ± 0.01 μm.   The accuracy was limited by an implicit $\pm 2 \times 10^{-4}$ uncertainty in n_o that exists in the commonly used Sellmeier equation of G. J. Edwards and M. Lawrence, Opt. Quantum Electron. **16**, 373 (1984).   For a pump wavelength $\lambda_p = 1064$ nm, fitting the model to the *e*-polarized fringes revealed that n_e at 532 nm deviated from the Sellmeier result by typically -1.58×10^{-4}.   The uniformity of n_e over a wafer 10 cm in diameter was approximately $\pm 4 \times 10^{-5}$.   This result is consistent with that expected from compositional variations.   Our model included multiple passes of the pump and second-harmonic waves.   The effects of photoelastic strain in producing perturbations and mixing of the *e*- and *o*-polarized fringes was investigated. This was restricted to two experimentally motivated cases that suggested that strains produce rotations of the optic axis by typically $\pm 0.05°$ about the *x* axis and *y* axis with the former assigned to an indeterminant combination of S_1, S_2, and S_4 and the latter to an indeterminant combination of S_5 and S_6.   In both cases the magnitude of the collective strains is of the order of 10^{-4}.   The birefringence variations that are due to strain are of the same magnitude as those expected from compositional variations.   The formalism developed here is used in the subsequent mapping study of *x*-cut wafers.   © 1998 Optical Society of America
[S0740-3224(98)00412-3]

OCIS codes: 160.3730, 160.4330, 190.1900, 190.4400.

1. INTRODUCTION

Maker fringes are defined as oscillations of the second-harmonic generation (SHG) intensity as a function of the transmitted pump-beam angle of incidence.   They have often been used as a means to comparatively measure the second-order susceptibility of nonlinear optical materials with respect to reference samples.[1]   To produce Maker fringes, a sample is typically rotated about a particular crystalline axis while a polarized pump beam illuminates a spot on the sample that falls on the rotation axis.   The SHG fringes are then continuously produced as the sample is rotated.   The character of the fringes, however, depends on the experimental orientation in terms of pump-beam polarization, choice of rotation axis, choice of the polarization of the SHG, wavelength of the pump, and so on.   In our analysis of the *x*-cut sample orientation presented in this paper we have chosen the geometry where the sample plate is rotated about an axis parallel to the *y*-axis while the pump polarization is also parallel to the *y*-axis.   With this orientation a single rotation scan will simultaneously produce both *e*- and *o*-polarized fringes that are dependent on the ordinary indices of refraction at the pump and SHG wavelengths, n_o^p and n_o, respectively, and on the extraordinary index at the SHG wavelength n_e.   The amplitude and oscillation of the *o*-polarized fringes depend on n_o, n_o^p, d_{22}, sample thickness, and pump power.   Similarly, the amplitude and os-

cillation of the *e*-polarized fringes depend on n_o, n_o^p, n_e, d_{31}, sample thickness, and pump power.   This choice of this sample orientation simplifies the analysis somewhat, since the pump is always an ordinary wave and only the *e*-polarized SHG is an extraordinary wave that depends on n_e, n_o, and n_o^p.   In LiNbO₃ the compositionally dependent variation in birefringence is primarily due to variations in n_e over the range in which the material is in a single phase.   Over the same compositional range, however, the ordinary index n_o is nearly independent of composition.[2]   Within this approximation the *o*-polarized Maker fringes may then be used to compute the sample thickness at the position on the sample where the scan was recorded.   The sample thickness data is then available for use as input for the analysis and for fitting of the *e*-polarized fringes.

The *e*-polarized fringes are sensitive to birefringence, owing to the orthogonal relation between the pump and the SHG polarizations.   Fitting the *e*-polarized data, which is collected from various remote positions about a sample, with our theoretical model has allowed us to resolve birefringence variations of the order of $\pm 5 \times 10^{-6}$. We recently published a preliminary description of Maker fringe analysis that described the mapping of birefringence variations across 100-mm-diameter, *x*-cut LiNbO₃ wafers.[3]   Variations of the birefringence in LiNbO₃ may be tied closely to variations in the Li/Nb mole ratio.[2]

This feature has been employed in studies of the temperature dependence of the phase matching for SHG and for optical parametric oscillation (OPO). The SHG and OPO studies were used to examine the composition dependence of the birefringence observed in conjunction with crystal growth and vapor-transport equilibration experiments.[4,5] Early work that suggested the use of Maker fringe analysis as a mapping scheme to examine the uniformity of LiNbO$_3$ wafers and boules was described by Lunt *et al.*[6]

The Maker fringe analysis is useful, however, in extracting more than just information on nonlinear susceptibility, sample thickness, birefringence, and associated compositional variations. For example, we recently reported the use of this technique in the study of domain-inverted z-cut LiNbO$_3$ samples and also showed that the analysis may be used to examine pyroelectric effects and processing history for z-cut material.[7,8] Effects that are due to photoelastic strain are also revealed in the Maker fringe data for x-cut LiNbO$_3$. For example, strain that is inherent in the material and that produces refractive-index variations in the range of 10^{-5}–10^{-4} has been observed with linear interferometry.[9] We consider the analysis of two cases involving photoelastic strain that are revealed in the Maker fringe data for the x-cut material. The first case deals with a strain-induced admixture of the dominant e-polarized SHG fringes into the weaker o-polarized fringes. This is modeled by consideration of strain-induced rotation of the optic axis about the x axis. The degree of admixture is directly related to the strain that produces the rotation of the optic axis. We found that the magnitude of the strain associated with this admixture is approximately 1×10^{-4}. Furthermore, the admixture can be associated with static axial strains S_1, S_2 and with static shear strain S_4. However, it is not possible to uniquely assign the contribution or sign of these strain components. The second photoelastic artifact involves a strain-induced rotation of the optic axis about the y axis. This effect is attributed to producing small asymmetric angular displacements (with respect to pump-beam angle of incidence θ_i) that are observed in the e-polarized fringes. These strain-induced fringe displacements may be distinguished from compositionally induced variations in birefringence, since the latter necessarily produce symmetric breathing of the fringes with respect to θ_i. The magnitude of the axis rotation that produces these asymmetric fringe displacements is approximately 0.05°, and the magnitude of the corresponding strain is approximately 5×10^{-5}. The effect is assigned to static S_5 and S_6 shear strains, but, as with the first example of photoelastic variations to the Maker fringes, it is not possible to uniquely assign the contribution of these two components. The analysis developed in this paper is subsequently used in a companion study that examines, in some detail, Maker fringe mapping of x-cut LiNbO$_3$ wafers that were sequentially cut from their host boules.[10]

2. DERIVATION AND SOLUTION OF THE NONLINEAR WAVE EQUATIONS

We consider the case of a single transmitted pump beam at frequency ω_p and wavelength λ_p that is polarized par-

allel to the LiNbO$_3$ y-axis while the plate is rotated about the y-axis. The geometry of the orientation is shown in Fig. 1. The y-polarized (that is, o-polarized) pump field results in both o- and e-polarized SHG fields at ω ($\omega = 2\omega_p$), owing to the nonlinear source polarization that has an o-polarized component P_y and an e-polarized component P_z. Figure 1 illustrates the interaction in terms of the wave vectors of the input pump field, the nonlinear source polarization in the media, and the SHG fields. All the fields are assumed to be plane waves of infinite transverse extent. The boundary conditions require that the amplitudes and phases of the components of the electric and magnetic fields parallel to the interfaces be continuous across the interfaces. These constraints result in the projections of the wave-vector components as illustrated in Fig. 1 and allow for the computation of the refraction angles θ_s (for the e-polarized SHG field), θ_p (for the o-polarized pump field), and ϕ_s (for the o-polarized SHG field), all in terms of the incident angle of the pump θ_i. Appendix A lists and defines the wave vectors, indices of refraction, electric- and magnetic-field components, nonlinear source polarizations, and other terms used in the description of the fields. The reader will find it convenient to refer to this appendix when reading the development of the formalism that follows.

The complex y-polarized pump field in the LiNbO$_3$ is

$$\mathbf{E}_y^{P,T_1} = \hat{y}TE_y^{P,i} \exp[i(\gamma_x^p x + \gamma_z^p z - \omega_p t)]. \quad (1)$$

The factor T is the Fresnel transmission coefficient for the pump-field amplitude. The components of the complex nonlinear source-polarization vector are obtained from the contraction of the third-rank tensor d_{ijk} with the second-rank tensor $E_j^{PT_1}E_k^{PT_1}$ and are given by

$$\mathbf{P} = (\hat{y}d_{22} + \hat{z}d_{31})(TE_y^{P,i})^2 \exp[i(k_x^P x + k_z^P z - \omega t)]. \quad (2)$$

The unit vectors $\hat{x}$, $\hat{y}$, and $\hat{z}$ are parallel to the principal axes of the crystal. The standard abbreviated notation in which the third-rank tensor d_{ijk} is represented as a 3 × 6 matrix with $d_{22} \equiv d_{222}$ and $d_{31} = d_{32} \equiv d_{322}$ was used.

Fig. 1. A schematic showing the wave vectors γ, $\mathbf{k}$, κ, $\mathbf{k}^s$, κ^s, $\mathbf{k}^P$, and the associated angles of incidence, reflection, and refraction for the input pump field, the reflected e- and o-polarized SHG fields, the transmitted e-polarized SHG field, the transmitted o-polarized SHG field, and the nonlinear source polarization, respectively.

A set of nonlinear wave equations describing the SHG may be derived from Maxwell's equations with the inclusion of the nonlinear source polarization given by Eq. (2). Maxwell's curl equations for nonmagnetic, nonabsorbing media are

$$\nabla \times \mathbf{H} = \epsilon_o \widetilde{\epsilon} \cdot \frac{\partial \mathbf{E}}{\partial t} + \frac{\partial \mathbf{P}}{\partial t}, \tag{3a}$$

$$\nabla \times \mathbf{E} = -\mu_o \frac{\partial \mathbf{H}}{\partial t}. \tag{3b}$$

The second-rank dielectric tensor $\widetilde{\epsilon}$ is diagonal in the system of coordinates in which x, y, and z conform to principal axes of the crystal. For uniaxial LiNbO$_3$, $n_o^2 = \epsilon_{11} = \epsilon_{22}$ and $n_e^2 = \epsilon_{33}$. In Section 3 we discuss photoelastic perturbations to the material in which ϵ_{ij} is no longer diagonal and in which the crystal is no longer uniaxial. In such cases a suitable transformation of coordinates must be performed to restore ϵ_{ij} to a diagonal form. The wave propagation is confined to the xz plane so that partial derivatives with respect to y vanish. The time dependence of the SHG fields are represented by $\mathbf{E}(x, y, z, t) = \mathbf{E}(x, y, z)\exp(-i\omega t)$ and $\mathbf{H}(x, y, z, t) = \mathbf{H}(x, y, z)\exp(-i\omega t)$. With the understanding that partial derivatives are taken with respect to the subscripted variable, Eq. (3) may be written in component form as

$$-\partial_z H_y = -i\omega\epsilon_o n_o^2 E_x, \tag{4a}$$

$$-\partial_x H_z + \partial_z H_x = -i\omega\epsilon_o n_o^2 E_y - i\omega P_y, \tag{4b}$$

$$\partial_x H_y = -i\omega\epsilon_o n_e^2 E_z - i\omega P_z, \tag{4c}$$

$$-\partial_z E_y = i\omega\mu_o H_x, \tag{4d}$$

$$-\partial_x E_z + \partial_z E_x = i\omega\mu_o H_y, \tag{4e}$$

$$\partial_x E_y = i\omega\mu_o H_z. \tag{4f}$$

The substitution of H_x and H_z from Eqs. (4d) and (4f) into Eq. (4b) leads to a linear inhomogeneous wave equation for E_y,

$$\partial_{xx}^2 E_y + \partial_{zz}^2 E_y + k^2 n_o^2 E_y = -\frac{k^2}{\epsilon_o} P_y. \tag{5}$$

The derivation of the corresponding wave equations for E_x and E_z requires slightly more work. Solving Eq. (4e) for H_y and substituting the result into Eqs. (4a) and (4c) results in two equations that contain terms proportional to the mixed partial derivatives $\partial_{xz}^2 E_z$ and $\partial_{xz}^2 E_x$. We eliminate these terms with the following procedure. The nonlinear medium is assumed to be charge free, and therefore $\nabla \cdot \mathbf{D} = 0$. In the presence of the nonlinear source polarization the electric displacement vector $\mathbf{D} = \epsilon_o \widetilde{\epsilon} \cdot \mathbf{E} + \mathbf{P}$ becomes

$$\mathbf{D} = \epsilon_o(\hat{x} n_o^2 E_x + \hat{y} n_o^2 E_y + \hat{z} n_e^2 E_z) + \hat{y} P_y + \hat{z} P_z. \tag{6}$$

Since $\partial_y \equiv 0$ in the present case, the constraint $\nabla \cdot \mathbf{D} = 0$ gives

$$\partial_x E_x = \frac{-1}{\epsilon_o n_o^2}(\epsilon_o n_e^2 \partial_z E_z + \partial_z P_z), \tag{7a}$$

$$\partial_z E_z = \frac{-1}{\epsilon_o n_e^2}(\epsilon_o n_o^2 \partial_x E_x + \partial_z P_z), \tag{7b}$$

which leads to

$$\partial_{zx}^2 E_x = \frac{-1}{\epsilon_o n_o^2}(\epsilon_o n_e^2 \partial_{zz}^2 E_z + \partial_{zz}^2 P_z), \tag{7c}$$

$$\partial_{xz}^2 E_z = \frac{-1}{\epsilon_o n_e^2}(\epsilon_o n_o^2 \partial_{xx}^2 E_x + \partial_{xz}^2 P_z). \tag{7d}$$

Note that the order of partial differentiation may be interchanged in Eqs. (7c) and (7d). Using Eqs. (7c) and (7d) and Eq. (4), we then derive the linear inhomogeneous wave equations for E_x and E_z, which are

$$\left(\frac{n_o}{n_e}\right)^2 \partial_{xx}^2 E_x + \partial_{zz}^2 E_x + k^2 n_o^2 E_x = -\frac{1}{\epsilon_o n_e^2} \partial_{xz}^2 P_z, \tag{8a}$$

$$\partial_{xx}^2 E_z + \left(\frac{n_e}{n_o}\right)^2 \partial_{zz}^2 E_z + k^2 n_e^2 E_z = -\frac{1}{\epsilon_o n_o^2} \partial_{zz}^2 P_z$$
$$-\frac{k^2}{\epsilon_0} P_z. \tag{8b}$$

The factor $\partial_{xz}^2 P_z$ is proportional to $d_{31}\sin(2\theta_p)$ and $\partial_{zz}^2 P_z$ and to $d_{31}\sin^2(\theta_p)$.

These terms are examples of effective nonlinear coefficients that are discussed by many authors in regard to cases in which the pump-beam polarization within the nonlinear medium does not conform to a principal dielectric axis.[11,12]

With the factors P_x, P_y, and P_z all zero, the fields E_x^h, E_y^h, and E_z^h that solve the homogeneous equations corresponding to Eqs. (5) and (8) are

$$E_x^h = E_x^o \exp[i(k_x^s x + k_z^s z - i\omega t)], \tag{9a}$$

$$E_y^h = E_y^o \exp[i(\kappa_x^s x + \kappa_z^s z - i\omega t)], \tag{9b}$$

$$E_z^h = E_z^o \exp[i(k_x^s x + k_z^s z - i\omega t)]. \tag{9c}$$

The extraordinary index as a function of θ_s, $n(\theta_s)$, is found by substitution of Eqs. (9a) and (9c) into Eqs. (8), where

$$n(\theta_s) = \left(\frac{n_e^2 n_o^2}{n_e^2 \sin^2 \theta_s + n_o^2 \cos^2 \theta_s}\right)^{1/2} \quad \text{or} \tag{10a}$$

$$\frac{1}{n^2(\theta_s)} = \frac{\sin^2 \theta_s}{n_o^2} + \frac{\cos^2 \theta_s}{n_e^2}, \tag{10b}$$

which is a well-known result from crystal optics, when the definition of θ_s is noted as given in Fig. 1.

We have constrained the problem to experimental regimes in which the pump field is assumed constant and undepleted as it traverses the nonlinear medium. The general solutions of Eqs. (5) and (8) are then found when particular solutions of the inhomogeneous equations are added to the respective homogeneous equations. These

general solutions representing the e- and o-polarized SHG fields propagating from $x = 0$ to $x = L$ are

$$E_x = \{E_x^o \exp[i(k_x^s x + k_z^s z)]$$
$$+ A_x \exp[i(k_x^p x + k_z^p z)]\}\exp(-i\omega t), \quad (11a)$$

$$E_y = \{E_y^o \exp[i(\kappa_x^s x + \kappa_z^s z)]$$
$$+ A_y \exp[i(k_x^p x + k_z^p z)]\}\exp(-i\omega t), \quad (11b)$$

$$E_z = \{E_z^o \exp[i(k_x^s x + k_z^s z)]$$
$$+ A_z \exp[i(k_x^p x + k_z^p z)]\}\exp(-i\omega t). \quad (11c)$$

The factors A_x, A_y, and A_z are found by direct substitution of Eqs. (11) into Eqs. (5) and (8), which yields

$$A_x = \frac{d_{31}(E_y^{P,i}T)^2 k_x^p k_z^p}{\epsilon_o n_e^2\left[k^2 n_o^2 - \left(\dfrac{n_o}{n_e} k_x^p\right)^2 - (k_z^p)^2\right]}, \quad (12a)$$

$$A_y = \frac{d_{22}(E_y^{P,i}T)^2}{\epsilon_o[(n_o^p)^2 - n_o^2]}, \quad (12b)$$

$$A_z = \frac{d_{31}(E_y^{P,i}T)^2[(k_z^p)^2 - (n_o k)^2]}{n_o^2 \epsilon_o\left[k^2 n_e^2 - \left(\dfrac{n_e}{n_o} k_z^p\right)^2 - (k_x^p)^2\right]}. \quad (12c)$$

Taken together, Eqs. (11) and (12) represent the general solution to the problem of SHG for the orientation shown in Fig. 1, where all the fields are plane waves and the pump field is undepleted as it propagates through the crystal. The results are derived directly from Maxwell's equations with the full birefringence of the media kept. The homogeneous solutions are consistent with the standard results from crystal optics. The dependence of the nonlinear interaction on the pump-beam polarization and propagation directions follow directly from the procedures used in deriving Eqs. (1)–(12) and may be generalized to arbitrary polarization and propagation directions in the uniaxial media.

To complete the solution and find the SHG within the nonlinear media, we solve for the homogeneous field amplitudes E_x^o, E_y^o, and E_z^o by evoking the boundary conditions, which require that the tangential components of $\mathbf{E}$ and $\mathbf{H}$ be continuous across the boundary at $x = 0$. The components of the complex electric field at ω generated on reflection from the first interface are

$$E_x^{R_1} = E_x^{(R_1)_o} \exp[i(-k_x x + k_z z - \omega t)], \quad (13a)$$

$$E_y^{R_1} = E_y^{(R_1)_o} \exp[i(-\kappa_x x + \kappa_z z - \omega t)], \quad (13b)$$

$$E_z^{R_1} = E_z^{(R_1)_o} \exp[i(-k_x x + k_z z - \omega t)]. \quad (13c)$$

The ratio of the homogeneous field amplitudes E_x^o and E_z^o is also required. We may compute this quantity from $\nabla \cdot \mathbf{D} = 0$ by using Eqs. (11a) and (11c) and setting $P_z = P_y = 0$. The ratio of the reflected homogeneous field amplitudes $E_x^{(R_1)_o}$ and $E_z^{(R_1)_o}$ is calculated in a similar manner. The results are

$$E_x^o = -\frac{n_e^2 k_z^s}{n_o^2 k_x^s} E_z^o, \quad (14a)$$

$$E_x^{(R_1)_o} = \frac{k_z}{k_x} E_z^{(R_1)_o}. \quad (14b)$$

At the first interface ($x = 0$) there is no input field at ω, but this is not so at the second interface ($x = L$). The boundary conditions that require the continuity of the tangential fields at $x = 0$ give

$$H_y^{R_1}\big|_{(x=0)} = H_y\big|_{(x=0)}, \quad (15a)$$

$$H_z^{R_1}\big|_{(x=0)} = H_z\big|_{(x=0)}, \quad (15b)$$

$$E_y^{R_1}\big|_{(x=0)} = E_y\big|_{(x=0)}, \quad (15c)$$

$$E_z^{R_1}\big|_{(x=0)} = E_z\big|_{(x=0)}. \quad (15d)$$

Equations (15) must be valid at any point on the line defined by $x = 0$ in Fig. 1. The transverse phases

$$\exp(ik_z^p z), \quad \exp(ik_z^s z), \quad \exp(ik_z z),$$
$$\exp(i\kappa_z^s z), \quad \exp(i\kappa_z z)$$

must therefore be equal at any point z on this line. This introduces the further constraint that $k_z^p = k_z^s = k_z = \kappa_z = \kappa_z^s$. From Eqs. (4e) and (4f) and Eqs. (14) and (15), the solutions for the electric-field amplitudes E_z^o, $E_z^{(R_1)_o}$, E_y^o, and $E_y^{(R_1)_o}$ are

$$E_z^o = \frac{A_x - [k_x^p/k_z + k_x/k_z + k_z/k_x]A_z}{[(n_e/n_o)^2 k_z/k_x^s + k_x^s/k_z + k_x/k_z + k_z/k_x]}, \quad (16a)$$

$$E_z^{(R_1)_o} = E_z^o + A_z, \quad (16b)$$

$$E_y^o = -A_y \frac{[\kappa_x + k_x^p]}{[\kappa_x + \kappa_x^s]}, \quad (16c)$$

$$E_y^{(R_1)_o} = A_y \frac{[\kappa_x^s - k_x^p]}{[k_x^s + \kappa_x]}. \quad (16d)$$

And E_x^o is then found from Eq. (14a).

The boundary conditions on the tangential fields allow the angles θ_R, θ_P, θ_S, and ϕ_S to all be expressible in terms of θ_i:

$$\theta_R = \theta_i, \quad (17a)$$

$$\sin \theta_P = \frac{\sin \theta_i}{n_o^p}, \quad (17b)$$

$$\sin \theta_S = \frac{n_o \sin \theta_i}{[(n_o n_e)^2 + (n_o^2 - n_e^2)\sin^2 \theta_i]^{1/2}}, \quad (17c)$$

$$\sin \phi_s = \frac{\sin \theta_i}{n_o}. \quad (17d)$$

If the media to the left-hand side of the boundary at $x = 0$ is substantially dispersive, then Eq. (17a) is not valid and the reflected pump and SHG fields will emerge at different angles. This fact was used in a classic example of the generation of SHG on boundary reflection.[13] For computation and display of the reflected and trans-

mitted fields, it is convenient to use the normalized factors $\bar{E}_x^{(R_1)_o} = E_x^{(R_1)_o}/N$, $\bar{E}_y^{(R_1)_o} = E_y^{(R_1)_o}/M$, $\bar{E}_z^{(R_1)_o} = E_z^{(R_1)_o}/N$, $\bar{A}_x = A_x/N$, $\bar{A}_y = A_y/M$ and $\bar{A}_z = A_z/N$ with M and N defined by

$$N = \frac{d_{31}}{\epsilon_o}(E_y^{P,i})^2, \tag{18a}$$

$$M = \frac{d_{22}}{\epsilon_o}(E_y^{P,i})^2. \tag{18b}$$

The pump-field amplitude in the nonlinear media is o polarized, and the corresponding Fresnel transmission coefficient T for the pump field is

$$T = \frac{2\cos\theta_i}{n_o^p\cos\theta_p + \cos\theta_i}. \tag{19}$$

The factors $\bar{A}_x$, $\bar{A}_y$, and $\bar{A}_z$ become

$$\bar{A}_x = \frac{T^2\sin 2\theta_p}{2n_e^2\left[\left(\dfrac{n_o}{n_o^p}\right)^2 - \left(\dfrac{n_o\cos\theta_p}{n_e}\right)^2 - \sin^2\theta_p\right]}, \tag{20a}$$

$$\bar{A}_y = \frac{T^2}{[(n_o^p)^2 - n_o^2]}, \tag{20b}$$

$$\bar{A}_z = \frac{T^2\left[\sin^2\theta_p - \left(\dfrac{n_o}{n_o^p}\right)^2\right]}{n_o^2\left[\left(\dfrac{n_e}{n_o^p}\right)^2 - \left(\dfrac{n_e\sin\theta_p}{n_o}\right)^2 - \cos^2\theta_p\right]}. \tag{20c}$$

The normalized reflected field amplitude $\bar{E}_z^{(R_1)_o} = \bar{E}_z^o + \bar{A}_z$ where the homogeneous field amplitude $\bar{E}_z^o$ reduces to

$$\bar{E}_z^o = \frac{\bar{A}_x - \bar{A}_z[\cot\theta_p + 2\csc 2\theta_i]}{\left[\left(\dfrac{n_e}{n_o}\right)^2\tan\theta_s + \cot\theta_s + 2\csc 2\theta_i\right]}. \tag{21}$$

The normalized e-polarized SHG power produced in reflection at $x = 0$ is defined by $\bar{P}_e^{R_1} = |\bar{E}_x^{(R_1)_o}|^2 + |\bar{E}_z^{(R_1)_o}|^2$ or

$$\bar{P}_e^{R_1} = |\bar{E}_z^{(R_1)_o}|^2\sec^2\theta_i. \tag{22}$$

The corresponding normalized o-polarized reflected SHG power is defined by $\bar{P}_o^{R_1} = |\bar{E}_y^{(R_1)_o}|^2$ and is given by

$$\bar{P}_o^{R_1} = (\bar{A}_y)^2\left[\frac{n_o\cos\phi_s - n_o^p\cos\theta_p}{n_o\cos\phi_s + \cos\theta_i}\right]^2. \tag{23}$$

Figure 2 illustrates a graph of both $\bar{P}_e^{R_1}$ and $\bar{P}_o^{R_1}$ as functions of θ_i for $\lambda_p = 1064$ nm and the sample temperature $T_s = 25\,°C$. The Sellmeier equations defined by Edwards and Lawrence, which rely on the refractive-index data of Nelson and Mikulyak, were used in the generation of all graphical results displayed in this paper.[14,15]

Figure 2 suggests that the SHG generated on surface reflection should be useful for measuring variations in d_{22} and d_{31} near the surface of a sample. Indeed, Bloembergen has shown that the surface-generated SHG arises
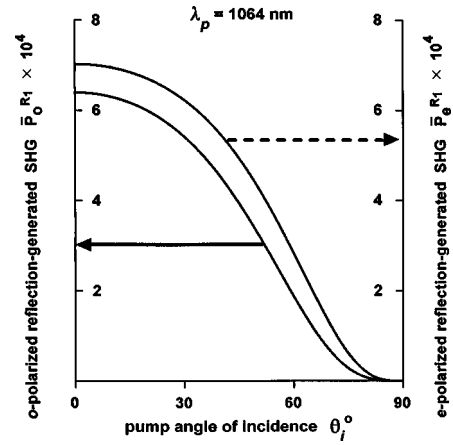
Fig. 2. The normalized e- and o-polarized SHG generated on reflection of the pump field at the first surface ($x = 0$) as a function of pump angle of incidence θ_i.

from a layer of radiating dipoles approximately λ in thickness.[16] Experimentally resolving such variations should be a simple matter. In practice, however, a flat sample plate with both surfaces polished and parallel renders such a direct measurement essentially impossible. This is because the combined reflections of the pump and forward-traveling SHG from the second surface together produce a strong backward-traveling SHG signal that cannot be separated from the reflection-generated SHG of the first surface. Surface-generated SHG was used to examine the reduction in $\chi^{(2)}$ suffered by proton-exchanged layers in LiNbO$_3$, where the samples were polished into a wedge shape to avoid the problems of second-surface reflections.[17] Our motivation in this paper, however, is to develop schemes for the analysis of LiNbO$_3$ plates routinely fabricated in production environments, and consideration of wedge-shaped samples is therefore not an option.

To obtain accurate fits of theory with data, we must consider the dependence of the Maker fringe patterns on multiple reflections of the pump and the SHG and on the divergence of the pump beam traversing the sample. In many practical situations in which the samples are approximately 1 mm in thickness and in which the focused beam diameter of the pump is in the range of 40–100 μm, the overlap and interference of multiple internal pump and SHG reflections will contribute to a fine structure in the Maker fringe patterns for θ_i within approximately $\pm 5°$ of the normal, since the plate will act as an interferometer. As illustrated below, these interferometric effects may drastically alter the envelope of the Maker fringes. Additionally, the scalar addition of the multiple SHG passes that occur for $|\theta_i| \geq 5°$ can still change the envelope of the Maker fringes by several percent. For cases of samples that are relatively thick with respect to the Gaussian confocal beam parameter of the pump, the effects of pump-beam divergence on the Maker fringe patterns must be considered. Beam-divergence effects have been described by Jerphagnon and Kurtz, who, nevertheless, did not consider the interferometric action of the sample in perturbing the Maker fringe envelopes.[1] Experimentally, however, we found that with the nominally 1-mm-thick samples of interest here, and with the range

of beam diameters given above, the effects of beam divergence do not noticeably perturb the envelopes of the Maker fringes. Thus, if the Maker fringe analysis is to be used for meaningful comparisons of the ratios of nonlinear optical coefficients, or if the fringe envelopes represent the quantity of interest in comparing various samples, then the envelopes must be accurately predicted and the appropriate correction factors included in the analysis. Indeed, it has recently come to our attention that the importance of including multiple passes of the pump and the SHG in measurements of d coefficients has been further verified by Shoji et al.[18]

We continue our treatment of the e- and o-polarized SHG fields for the crystal orientation shown in Fig. 1 by first considering a single pass of the pump and SHG fields through the crystal. We then compute corrections to the reflected and transmitted SHG fields that emerge from the sample plate by including contributions from multiple Fresnel reflections of the pump and the SHG. The components of the e-polarized SHG field incident on the boundary at $x = L$ from $x < L$ are given by Eqs. (11a) and (11c). The geometry of this situation is illustrated in Fig. 3. The general solutions for the e-polarized SHG fields propagating from $x = L$ to $x = 0$ are given by

$$E_x^{R_2} = (E_x^{(R_2)_o} \exp\{i[k_x^s(-x + L) + k_z^s z]\}$$
$$+ A_x^{(2)} \exp\{i[k_x^p(-x + L) + k_z^p z]\})\exp(-i\omega t),$$
$$(24a)$$
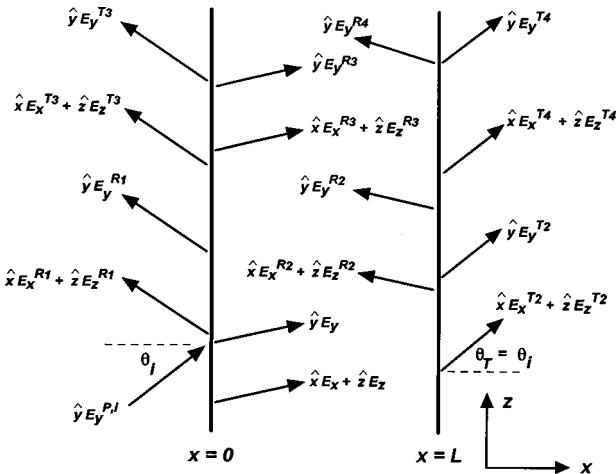
Fig. 3. A schematic showing the fields retained when we consider multiple reflections of the SHG. At $x = 0$ the y-polarized pump field $E_y^{P,i}$ produces y-polarized reflected field $E_y^{R_1}$, x-polarized reflected field $E_x^{R_1}$, z-polarized reflected field $E_z^{R_1}$, y-polarized transmitted field E_y, x-polarized transmitted field E_x, and z-polarized transmitted field E_z. These fields reflected and transmitted at $x = L$ produce the associated fields superscripted by R_2 and T_2, respectively. These latter fields, when reflected and transmitted from the boundary at $x = 0$, produce the fields superscripted by R_3 and T_3, respectively. Finally, with reflection and transmission at the boundary $x = L$, the R_3 and T_3 superscripted fields produce the R_4 and T_4 superscripted fields, respectively.

$$E_z^{R_2} = (E_z^{(R_2)_o} \exp\{i[k_x^s(-x + L) + k_z^s z]\}$$
$$+ A_z^{(2)} \exp\{i[k_x^p(-x + L) + k_z^p z]\})\exp(-i\omega t).$$
$$(24b)$$

The components of the e-polarized SHG field transmitted through the boundary at $x = L$ are given by

$$E_x^{T_2} = E_x^{(T_2)_o} \exp\{i[k_x(x - L) + k_z z]\}\exp(-i\omega t),$$
$$(25a)$$

$$E_z^{T_2} = E_z^{(T_2)_o} \exp\{i[k_x(x - L) + k_z z]\}\exp(-i\omega t).$$
$$(25b)$$

The input and output surfaces of the crystal are assumed parallel. The continuity of the transverse phases of the fields at $x = L$ requires $\sin \theta_i = \sin \theta_T$ or $\theta_T = \theta_i$, and the magnitudes of the wave-vector components k_x and k_z appearing in Eqs. (25) are thus the same as those for the SHG fields reflected from the boundary at $x = 0$. The factors $A_x^{(2)}$ and $A_z^{(2)}$ describing the inhomogeneous solutions of the e-polarized SHG fields traveling from $x = L$ to $x = 0$ are found by insertion of Eqs. (24a) and (24b) into Eqs. (8a) and (8b), respectively. The results are

$$A_x^{(2)} = -A_x R^2,$$
$$(26a)$$

$$A_z^{(2)} = A_z R^2.$$
$$(26b)$$

The factor R^2 is the square of the Fresnel (internal) reflection coefficient of the o-polarized pump field at the crystal–air interface and is given by

$$R^2 = \left[\frac{n_o^p \cos \theta_p - \cos \theta_i}{n_o^p \cos \theta_p + \cos \theta_i}\right]^2.$$
$$(27)$$

The continuity of the tangential field components at the boundary $x = L$ require

$$E_z|_{(x=L)} + E_z^{R_2}|_{(x=L)} = E_z^{T_2}|_{(x=L)},$$
$$(28a)$$

$$H_y|_{(x=L)} + H_y^{R_2}|_{(x=L)} = H_y^{T_2}|_{(x=L)}.$$
$$(28b)$$

These equations are solved in a manner similar to that used for the e-polarized SHG field reflected from the first surface as given above in the discussion surrounding Eqs. (15). The solution for the e-polarized component $E_z^{(T_2)_o}$ is

$$E_z^{(T_2)_o} = b_1 E_z^o \exp(ik_x^s L) + (A_z b_2 + A_x b_3)\exp(ik_x^p L)$$
$$+ [A_z^{(2)} b_4 + A_x^{(2)} b_3].$$
$$(29)$$

The factors b_1–b_4 are given by

$$b_1 = \left[\frac{2a_1}{a_1 + a_2}\right],$$
$$(30a)$$

$$b_2 = \left[\frac{a_1 + k_x^p}{a_1 + a_2}\right],$$
$$(30b)$$

$$b_3 = \left[\frac{-k_z^p}{a_1 + a_2}\right],$$
$$(30c)$$

$$b_4 = \left[\frac{a_1 - k_x^p}{a_1 + a_2}\right],$$
$$(30d)$$

$$a_1 = \left[k_x^s + \left(\frac{n_e}{n_o}\right)^2 \frac{(k_z^s)^2}{k_x^s}\right],$$
$$(30e)$$

$$a_2 = \left[k_x + \frac{k_z^2}{k_x}\right]. \tag{30f}$$

The normalized e-polarized SHG power $\bar{P}_e^{T_2}$ leaving the crystal at $x = L$ is given by $\bar{P}_e^{T_2} = |\bar{E}_z^{(T_2)_o}|^2 + |\bar{E}_x^{(T_2)_o}|^2$ or

$$\bar{P}_e^{T_2} = \{H_1^2 + H_2^2 + H_3^2 + 2H_1 H_3 \cos(k_x^s L)$$
$$+ 2H_2 H_3 \cos(k_x^p L)$$
$$+ 2H_1 H_2 \cos[(k_x^s - k_x^p)L]\}\sec^2 \theta_i. \tag{31}$$

The factors H_1–H_3 (which should not be confused with magnetic field amplitudes) are defined by

$$H_1 = \bar{E}_z^o b_1, \tag{32a}$$

$$H_2 = (\bar{A}_z b_2 + \bar{A}_x b_3), \tag{32b}$$

$$H_3 = [\bar{A}_z^{(2)} b_4 + \bar{A}_x^{(2)} b_3]. \tag{32c}$$

The normalized field amplitudes $\bar{E}_x^{(T_2)_o}$, $\bar{E}_z^{(T_2)_o}$ and factors $\bar{A}_x^{(2)}$, $\bar{A}_z^{(2)}$ are defined by $E_x^{(T_2)_o}/N$, $E_z^{(T_2)_o}/N$, $A_x^{(2)}/N$, and $A_z^{(2)}/N$, respectively. Figure 4(a) is a graph of Eq. (31) for $\lambda_p = 1064$ nm, $L = 1$ mm, and the crystal temperature $T_s = 25$ °C. Equation (31) represents the first level of approximation (single pass of pump and SHG) in the use of Maker fringe analysis to examine birefringence variations in LiNbO$_3$ plates.

Graphical examples of Eq. (31) illustrate the sensitivity of the Maker fringes to small changes in birefringence. For simplicity, we regard deviations in the birefringence calculated from the Sellmeier equations as arising entirely from variations in n_e. This is motivated by the sensitivity of n_e (and the insensitivity of n_o) to fluctuations in the Li/Nb mole ratio.[2] The extraordinary index at the second-harmonic wavelength derived from the Sellmeier equation is defined as n_e^s. We introduce the factor $\Delta^s n_e = n_e - n_e^s$, which represents a deviation of n_e from the value obtained from the Sellmeier equation. In this regard Fig. 4(b) illustrates the sensitivity of Eq. (31) to variations in n_e with consideration of $\Delta^s n_e = 5 \times 10^{-6}$ and $\Delta^s n_e = 2 \times 10^{-5}$. The magnitude of both H_1 and H_2 at normal incidence is ~58, and the magnitude of H_3 is ~0.004. The factors involving H_3 may therefore be ignored. Graphs of Eq. (31) at the pump wavelengths 1319 and 1090 nm, the latter of which permits critical phase matching, are shown in Figs. 4(c) and 4(e), respectively. Clearly, since our formalism was derived in the approximation that neglected pump depletion, a general application of Eq. (31) to predict the normalized SHG power near the phase-matching peak indicated in Fig. 4(e), for arbitrary values of pump-beam diameter and sample thickness, is problematic. Nevertheless, the model is useful in the regime of limited conversion efficiency and may be used to locate the angular position θ_{pm} of critical phase-matching peaks in any case. In Fig. 4(f) we include an example that illustrates the variation of θ_{pm} for $\Delta^s n_e = 2 \times 10^{-5}$. A comparison of Figs. 4(a)–4(f) reveals that the Maker fringe patterns produced by all three pump wavelengths display comparable sensitivity to $\Delta^s n_e = 2 \times 10^{-5}$. Interestingly, Fig. 4(f) shows that for samples 1 mm thick, no particular advantage is gained, in

terms of using a fringe shift to detect a variation in birefringence $\Delta^s n_e$, with operation at a pump wavelength that yields a critical phase-matching angle. Indeed, the shift in θ_{pm} is only approximately $-0.11°$ for $\Delta^s n_e = 2 \times 10^{-5}$ and $\lambda_p = 1090$ nm.

We now compute the case of a single pass of the pump and SHG that produces o-polarized SHG fringes and compare the relative SHG power with the corresponding e-polarized fringes. The o-polarized field incident from the left on the boundary at $x = L$ is given by Eq. (11b). The geometry of this situation is illustrated in Fig. 3. The general solution for the o-polarized SHG field propagating from $x = L$ to $x = 0$ is

$$E_y^{R_2} = (E_y^{(R_2)_o} \exp\{i[\kappa_x^s(-x + L) + \kappa_z^s z]$$
$$+ A_y^{(2)} \exp\{i[k_x^p(-x + L) + k_z^p z]\})\exp(-i\omega t), \tag{33}$$

where $A_y^{(2)} = A_y R^2$. The o-polarized SHG field transmitted through the boundary at $x = L$ is given by

$$E_y^{T_2} = E_y^{(T_2)_o} \exp\{i[\kappa_x(x - L) + \kappa_z z]\}\exp(-i\omega t). \tag{34}$$

Continuity of the tangential fields at $x = L$ requires

$$E_y|_{(x=L)} + E_y^{R_2}|_{(x=L)} = E_y^{T_2}|_{(x=L)}, \tag{35a}$$

$$H_z|_{(x=L)} + H_z^{R_2}|_{(x=L)} = H_z^{T_2}|_{(x=L)}. \tag{35b}$$

Note that H_z, $H_z^{R_2}$, and $H_z^{T_2}$ are found by use of Eq. (4f). The normalized o-polarized SHG leaving the plate at $x = L$ is given by $\bar{P}_o^{T_2} = |\bar{E}_y^{(T_2)_o}|^2$, where $\bar{E}_y^{(T_2)_o} = E_y^{(T_2)_o}/M$ and

$$\bar{E}_y^{(T_2)_o} = G_1 \exp(i\kappa_x^s L) + G_2 \exp(ik_x^p L) + G_3. \tag{36}$$

$\bar{P}_o^{T_2}$ then becomes

$$\bar{P}_o^{T_2} = G_1^2 + G_2^2 + G_3^2 + 2G_1 G_3 \cos(\kappa_x^s L)$$
$$+ 2G_2 G_3 \cos(k_x^p L) + 2G_1 G_2 \cos[(\kappa_x^s - k_x^p)L]. \tag{37}$$

The factors G_1–G_3 are given by

$$G_1 = \left[\frac{2\kappa_x^s}{\kappa_x^s + k_x}\right]\bar{E}_y^o, \tag{38a}$$

$$G_2 = \left[\frac{k_x^p + \kappa_x^s}{k_x + \kappa_x^s}\right]\bar{A}_y, \tag{38b}$$

$$G_3 = \left[\frac{\kappa_x^s - k_x^p}{k_x + \kappa_x^s}\right]\bar{A}_y^{(2)}, \tag{38c}$$

with $\bar{A}_y^{(2)} = A_y^{(2)}/M$. A graph of Eq. (37) is shown in Fig. 5(a) for $\lambda_p = 1064$ nm, $L = 1$ mm, and $T_s = 25$ °C. Equation (37) is useful for many practical applications that involve the mapping of thickness variations across a LiNbO$_3$ plate with o-polarized Maker fringe data. Figure 5(b) illustrates the sensitivity of Eq. (37) to a variation in L of 0.1 μm. At normal incidence the magnitude of the factors G_1 and G_2 is ~1.26 and the magnitude of G_3 is ~0.0037. Consequently, high-frequency fringes propor-
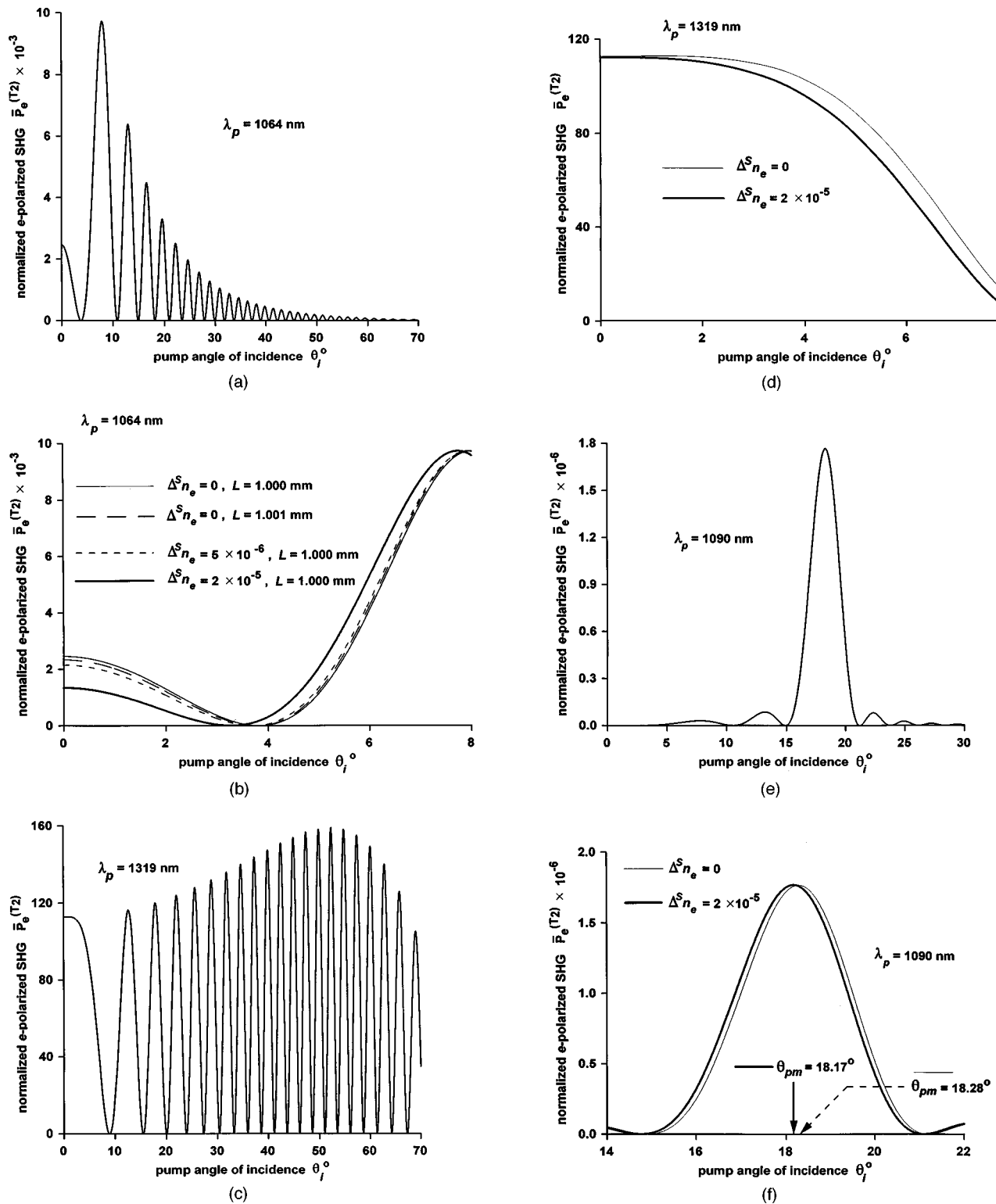
Fig. 4.   (a) The normalized e-polarized SHG power $\bar{P}_e^{(T_2)}$ as a function of pump angle of incidence θ_i for $\lambda_p = 1064$ nm, $T_s = 25$ °C and $L = 1$ mm.   (b) Graphs showing normalized e-polarized SHG $\bar{P}_e^{(T_2)}$ as a function of pump angle of incidence θ_i for $\lambda_p = 1064$ nm, which compare the sensitivity of the fringe patterns with small changes in birefringence and thickness.   The result shows that a deviation $\Delta^s n_e = 5 \times 10^{-6}$ of n_e from the Sellmeier result may be resolved but that variations in sample thickness of ± 1 μm near $L = 1$ mm are not resolved. $T_s = 25$ °C for all graphs shown. (c) $\bar{P}_e^{(T_2)}$ for $\lambda_p = 1319$ nm, $T_s = 25$ °C and $L = 1$ mm.   (d) Graph illustrating the sensitivity of $\bar{P}_e^{(T_2)}$ to a variation $\Delta^s n_e = 2 \times 10^{-5}$ for $\lambda_p = 1319$ nm, $T_s = 25$ °C, and $L = 1$ mm.   (e) Graph illustrating the critical phase matching peak for $\lambda_p = 1090$ nm, $T_s = 25$ °C, and $L = 1$ mm.   (f) Graphs illustrating the shift in the critical phase matching angle θ_{pm} that is due to a variation $\Delta^s n_e = 2 \times 10^{-5}$ for $\lambda_p = 1090$ nm, $T_s = 25$ °C, and $L = 1$ mm.

tional to cos $k_x^p L$ and cos $\kappa_x^s L$ occur, but they contribute to an amplitude perturbation of only approximately 0.3%.

A number of factors must be considered for the practical application of Maker fringe analysis to the examination of birefringence variations in LiNbO$_3$. For example, the conversion efficiency should be strong enough that an adequate signal-to-noise ratio exists but not so strong that photorefractive instabilities are a problem. Indeed, since it is desirable to examine production wafers that are ~10 cm in diameter, the notion of maintaining a wafer at a precisely defined temperature, as may be required for maintaining phase matching, or of continuously annealing out photorefractive damage at elevated temperatures is impractical. A particular concern was that photorefractive coupling between e- and o-polarized SHG similar to effects reported in LiNbO$_3$ wave-guide devices would occur.[19] Experimentally, however, we found that with $\lambda_p = 1064$ nm, pump powers in the range of 700 mW–1 W, and pump-beam diameters in the range of 50–100 μm, sufficient power for both the e- and o-polarized SHG was produced without introduction of photorefractive instabilities. We arrived at this conclusion by observing that

repetitive scans at a single location on a sample would continue to produce the same e- and o-polarized fringe patterns within the experimental error. For the data presented in this paper, the continuous-wave pump was chopped at 800 Hz and the SHG was detected with a photomultiplier tube and a lock-in amplifier.

As is discussed in more detail in Section 4, another issue of practical concern involves photoelastic strain. For $\lambda_p = 1064$ nm, comparison of Figs. 4(a) and 5(a) reveals that the relative intensity ratio of the e- and o-polarized fringe patterns is approximately 1000:1. Thus, to resolve the weaker o-polarized signal, the dominant e-polarized signal must be rejected with a polarizer of suitable quality. We found that with the polarizer set to reject the e-polarized SHG for a scan taken at a particular location on the sample, translating the sample a few millimeters along y or z and repeating the scan would often reveal corruption of the o-polarized fringes by the mixture of extra fringes that corresponded exactly to the e-polarized SHG. Thus the extinction condition necessary for resolving the weaker o-polarized signal by rejection of the dominant e-polarized signal varied across the sample. The corre-
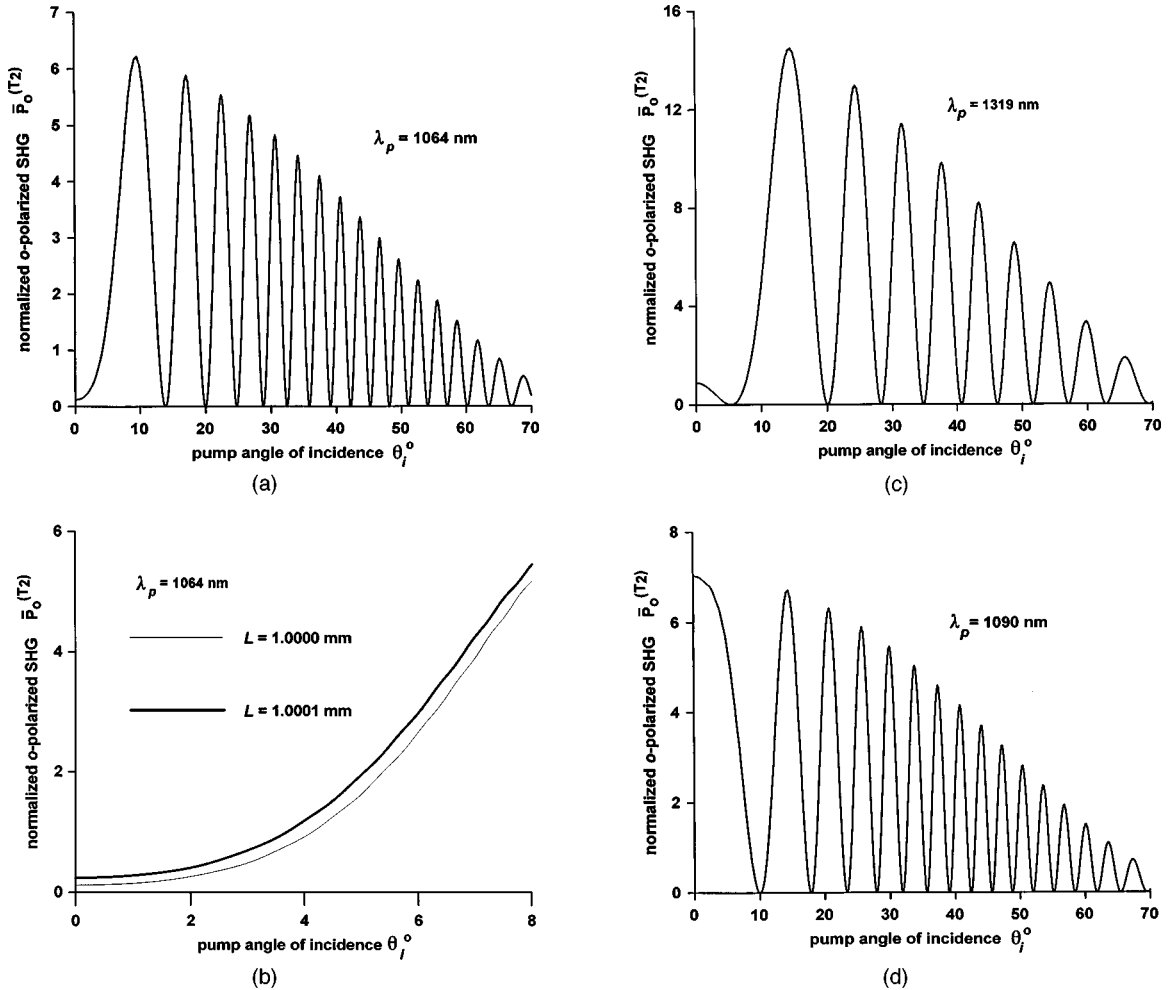
Fig. 5.   (a) Normalized o-polarized SHG $\bar{P}_o^{(T_2)}$ as a function of θ_i for $\lambda_p = 1064$ nm, $T_s = 25\,°$C and $L = 1$ mm.   (b) $\bar{P}_o^{(T_2)}$ illustrating the resolution of thickness variations where $L = 1$ mm $\pm$ 0.1 μm.   (c) Normalized o-polarized SHG $\bar{P}_o^{(T_2)}$ as a function of θ_i for $\lambda_p = 1319$ nm, $T_s = 25\,°$C, and $L = 1$ mm.   (d) Normalized o-polarized SHG $\bar{P}_o^{(T_2)}$ as a function of θ_i for $\lambda_p = 1090$ nm, $T_s = 25\,°$C and $L = 1$ mm.

sponding variation in the polarizer orientation was approximately $\pm 0.1°$. We attributed these effects to strain-induced photoelastic perturbations in the samples. In Section 4 we demonstrate that strains of the order of 10^{-5} are sufficient to induce a small rotation of the optic axis about the x-axis, which results in the leakage artifacts observed. Photoelastic variations in birefringence on this order were observed in LiNbO$_3$ by means of measuring wave-front distortion.[9]

A comparison of Figs. 4 and 5 reveals that the pump wavelength $\lambda_p = 1064$ nm, in addition to being conveniently obtained from a Nd:YAG laser, fortuitously provides better resolution of these strain artifacts than the other pump wavelengths considered. For example, for $\lambda_p = 1319$ nm, the intensity ratio between the e- and o-polarized Maker fringes is approximately 10:1, so a leakage effect arising from strains of the order of 10^{-5} would be difficult to resolve. The intensity ratio between the e- and o-polarized SHG signals for the case of $\lambda_p = 1090$ nm, which gives a critical phase-matching condition, results in an intensity ratio of approximately 2.4×10^5:1. This higher ratio would provide resolution of photoelastic artifacts that are improved over those of $\lambda_p = 1064$ nm; however, it would also require a polarizer with an extinction ratio of approximately 10^6:1 in order to permit resolution of the o-polarized signal. Such high-extinction polarizers are often difficult to obtain commercially. Finally, the increased SHG efficiency near the phase-matching peak may result in photorefractive perturbations that counteract the increase in sensitivity.

Considering all of these factors (sample thickness measurements, photorefractive effects, photoelastic strain, and birefringence variations), selecting $\lambda_p = 1064$ nm conveniently enables the measurement of birefringence and strain effects simultaneously. Finally, the model for the o-polarized Maker fringe patterns applies equally well to a z-cut plate rotated about the y-axis for the pump polarization aligned with the rotation axis. An example is shown in Section 3, in which multiple-pump and SHG passes are considered.

3. CORRECTIONS TO THE MAKER FRINGE PATTERNS THAT ARE DUE TO MULTIPLE REFLECTIONS OF THE PUMP AND THE SECOND-HARMONIC GENERATION

The approximation described in Section 2 is sufficient for many practical applications of Maker fringe analysis for the measurement of LiNbO$_3$ uniformity. Experimentally, however, we find that the structure of both the e- and o-polarized Maker fringe patterns are more complex than the results revealed in Figs. 4 and 5. Additional structure that is due to the multiple internal reflections of both the pump and the SHG appears in the fringes. This is particularly evident near $\theta_i = 0$. Furthermore, the envelopes of the Maker fringe patterns are significantly changed by the inclusion of multiple reflections. Therefore, if the analysis is to be used for accurate comparison of nonlinear optical coefficients, allowance for these multiple-reflection effects must be included. Given typical sample thicknesses of ~1 mm and pump-beam diam-

eters in the range of 40–100 μm, the summation of these reflections is complicated by the fact that they pass from a regime of overlap and interference to that of scalar addition as the plate is rotated approximately 5° from $\theta_i = 0$. In addition, in wafer-mapping experiments that use Maker fringe analysis to track wafer thickness and birefringence variations, it is desirable to save time by minimization of the scan range of θ_i. Inclusion of these multiple-pass corrections is therefore essential in order to accurately fit the Maker fringe data in the vicinity of $\theta_i = 0$. In practice we find that the inclusion of just two passes of the pump and three passes of the SHG is sufficient to fit the e- and o-polarized fringe data to high accuracy. Figures illustrating superpositions of the experimental data with the results of this improved modeling are described below. Therefore, given the success and flexibility of these approximations for the cases of practical interest described in this paper, we found it unnecessary to resort to the more general transfer-matrix approach described by Bethune.[20]

A. o-Polarized Maker Fringes Corrected for Multiple Internal Reflections

We now compute the additional o-polarized fields that arise from multiple reflections of the pump and SHG as illustrated in Fig. 3. Continuity of the y-polarized SHG fields at $x = L$ requires that $E_y^{(R_2)_o}$ be given by

$$E_y^{(R_2)_o} = E_y^{(T_2)_o} - E_y^o \exp(i\kappa_x^s L) - A_y \exp(ik_x^p L) - A_y^{(2)}. \tag{39}$$

We ignore factors proportional to G_3 that appear in the expression for $E_y^{(T_2)_o}$ in keeping with the approximations established in Section 2. The fields transmitted and reflected from the surface at $x = 0$ that are due to the incident field $E_y^{(R_2)}$ propagating in the $-x$ direction are

$$E_y^{(T_3)} = E_y^{(T_3)_o} \exp[i(-k_x x + k_z z - \omega t)], \tag{40a}$$

$$E_y^{(R_3)} = E_y^{(R_3)_o} \exp[i(\kappa_x^s x + \kappa_z^s z - \omega t)]. \tag{40b}$$

Terms proportional to R^2 are retained, but factors involving higher powers of R are neglected. Thus Eq. (39) includes the contribution of the first backward pass of the pump field within the term $A_y^{(2)}$, whereas Eq. (40b) neglects the second forward pass of the pump. The fields reflected and transmitted at $x = L$ due to the incident field $E_y^{(R_3)}$ arising from the second forward pass of the SHG are then

$$E_y^{(T_4)} = E_y^{(T_4)_o} \exp\{i[k_x(x - L) + k_z z - \omega t]\}, \tag{41a}$$

$$E_y^{(R_4)} = E_y^{(R_4)_o} \exp\{i[\kappa_x^s(L - x) + \kappa_z^s z - \omega t]\}. \tag{41b}$$

We arrive at a simple expression for $E_y^{(T_4)_o}$:

$$E_y^{(T_4)_o} = T_o R_o E_y^{(R_2)_o} \exp(2i\kappa_x^s L). \tag{42}$$

The factors T_o and R_o are the Fresnel transmission and reflection coefficients, respectively, for the o-polarized SHG fields, which are given by

$$T_o = \frac{2n_o \cos \phi_s}{(n_o \cos \phi_s + \cos \theta_i)}, \quad (43a)$$

$$R_o = \left[\frac{n_o \cos \phi_s - \cos \theta_i}{n_o \cos \phi_s + \cos \theta_i}\right]. \quad (43b)$$

T_o appears implicitly in the factor G_1. The normalized field amplitude $\bar{E}_y^{(T_4)_o} = E_y^{(T_4)_o}/M$ may be expressed as

$$\bar{E}_y^{(T_4)_o} = g_1 \exp(i3\kappa_x^s L) + g_2 \exp[i(2\kappa_x^s + k_x^p)L]$$
$$+ g_3 \exp(i2\kappa_x^s L), \quad (44)$$

with the factors g_1, g_2, and g_3 given by

$$g_1 = T_o R_o (G_1 - \bar{E}_y^o), \quad (45a)$$

$$g_2 = T_o R_o (G_2 - \bar{A}_y), \quad (45b)$$

$$g_3 = -T_o R_o \bar{A}_y^{(2)}. \quad (45c)$$

For a pump wavelength of 1064 nm at $\theta_i = 0$, the magnitudes of g_1, g_2, and g_3 are approximately 0.2, 0.2, and 0.075, respectively. Under the same conditions, the magnitudes of G_1 and G_2, which describe $\bar{E}_y^{(T_2)_o}$ for the single-pass case, were both approximately 1.26. Thus $\bar{E}_y^{(T_4)_o}$ provides a significant correction factor to the normalized o-polarized SHG field emerging from the plate at $x = L$, and the three terms g_1, g_2, and g_3 should be retained.

We now consider corrections to the o-polarized Maker fringe patterns that are due to the interference of multiple internal reflections of the pump field $TE_y^{P,i}$ and the interference of $E_y^{(T_2)_o}$ with $E_y^{(T_4)_o}$. The multiple internal reflections of the finite-diameter pump beam are considered first. The pump field is assumed to have a transverse Gaussian profile with a beam diameter of 2δ and an amplitude in the nonlinear medium of $TE_y^{P,i}$. As illustrated in Fig. 6, only two internal reflections of the pump are considered such that the pump field propagating in the $+x$ direction within the sample is composed of a primary component, owing to the first pass, and a secondary component that is reduced in amplitude from the primary component by two Fresnel reflections. A crucial assumption in this development is that the pump beam remains essentially collimated at its minimum Gaussian diameter
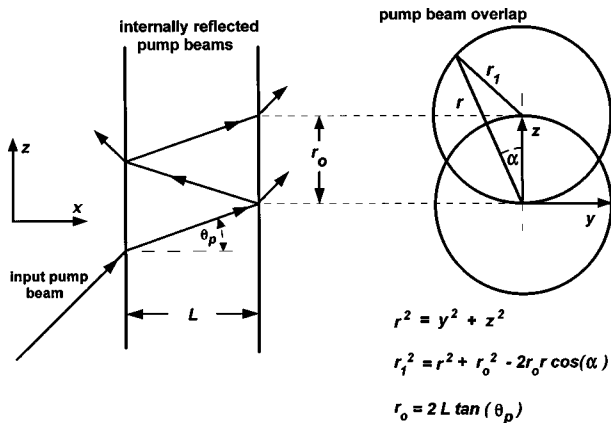
Fig. 6. Representation of overlapping multiple reflections of the Gaussian pump beam. Elliptical distortions of the pump-beam profile are ignored.

even after the two internal reflections. This assumption is valid provided that L is approximately $10\times$ less than the Gaussian focus parameter, or $L \le (\pi n_o^p \delta^2/10\lambda_p)$. Therefore, with the typical experimental conditions of $L \le 1$ mm, 70 μm $< 2\delta < 100$ μm, $n_o^p \sim 2.2$, and $\lambda_p = 1064$ nm, the divergence of the pump beam should not be a complicating issue. The overlap of the primary and secondary components of the pump field will depend on θ_p, the Fresnel reflection coefficient R at λ_p, and the spatial displacement of the two beams r_o. We represent the overlap heuristically by constructing an equivalent Gaussian pump beam with amplitude $E_y^{P,c}$ defined by

$$E_y^{P,c} \exp\left(-\frac{r^2}{\delta^2}\right) = TE_y^{P,i}\left\{\exp\left(-\frac{r^2}{\delta^2}\right)\right.$$
$$\left. + R^2 \exp\left(-\frac{r_1^2}{\delta^2}\right)\exp(i2k_x^p L)\right\}, \quad (46a)$$

$$r_1^2 = r^2 + r_o^2 - 2rr_o \cos \alpha, \quad (46b)$$

$$r_o = 2L \tan \theta_p, \quad (46c)$$

$$r^2 = y^2 + z^2. \quad (46d)$$

$E_y^{P,c}$ may be transformed into a convenient form by computing the power carried in the pump field P_y^p where only terms of R^2 are retained. Using the right-hand side of Eq. (46a), we find that

$$P_y^p = \frac{n_o^p}{2}[TE_y^{P,i}]^2 \left(\frac{\epsilon_o}{\mu_o}\right)^{1/2} \int_0^{2\pi}\int_0^{\infty}\left\{\exp\left(\frac{-2r^2}{\delta^2}\right)\right.$$
$$\left. + 2[\cos(2k_x^p L)]R^2 \exp\left(-\frac{r^2 + r_1^2}{\delta^2}\right)\right\}r\,dr\,d\alpha. \quad (47)$$

Equating P_y^p with the power computed by using the left-hand side of Eq. (46a) gives

$$|E_y^{P,c}|^2 = (TE_y^{P,i})^2[1 + 2R^2\phi \cos(2k_x^p L)], \quad (48a)$$

$$\phi = \exp[-(2L \tan \theta_p/\delta)^2]. \quad (48b)$$

Finally, we write the complex field amplitude $E_y^{P,c}$ as

$$E_y^{P,c} = TE_y^{P,i}\eta, \quad (49a)$$

$$\eta = [1 + R^2\phi \exp(i2k_x^p L)]. \quad (49b)$$

The effect of the internally reflected pump on the normalized e- and o-polarized SHG output is to introduce a complex correction term to $[E_y^{P,c}]^2$ that vanishes when θ_p is sufficiently large such that the internally reflected pump fields do not significantly overlap. For plates nominally 1 mm thick and for typical pump beam diameters in the range of 70–100 μm, the overlap becomes negligible for $|\theta_i| > 5°$. The correction factor η may be regarded simply as a modification of the Fresnel transmission coefficient T for the pump and thus is included as a multiplicative correction factor to the terms $\bar{A}_x$, $\bar{A}_y$, and $\bar{A}_z$. For $\delta \gg L$, $\phi \sim 1$ and Eq. (49b) reduces to the intuitive result for infinite plane waves.

We account for the interference of the overlapping fields $E_y^{(T_2)_o}$ and $E_y^{(T_4)_o}$ by computing the o-polarized SHG

power P_o, leaving the sample at $x = L$. Here $E_y^{(T_2)_o}$ and $E_y^{(T_4)_o}$ are treated as the amplitudes of Gaussian beams of diameter δ_s, where

$$P_o = \frac{1}{2}\left(\frac{\epsilon_o}{\mu_o}\right)^{1/2}\left\{\int_0^{2\pi}\int_0^\infty [|E_y^{(T_2)_o}|^2 + |E_y^{(T_4)_o}|^2]\right.$$

$$\times \exp\left(-\frac{2r^2}{\delta_s^2}\right)r\,dr\,d\alpha + 2\,\text{Re}\int_0^{2\pi}\int_0^\infty E_y^{(T_2)_o}(E_y^{(T_4)_o})^*$$

$$\left.\times \exp\left[-\frac{(r^2 + r_1^2)}{\delta_s^2}\right]r\,dr\,d\alpha\right\}. \tag{50}$$

We included the relationship between the Gaussian SHG and the pump-beam diameters, where $\delta_s\sqrt{2} = \delta$. We define the normalized o-polarized SHG power $\bar{P}_o$, which is corrected for both overlapping pump and SHG fields, leaving the plate at $x = L$ as

$$\bar{P}_o = (|\bar{E}_y^{(T_2)_o}|^2 + 2\,\text{Re}\{\bar{E}_y^{(T_2)_o}[\bar{E}_y^{(T_4)_o}]^*\}\phi_o$$

$$+ |\bar{E}_y^{(T_4)_o}|^2)|(\eta)^2|^2, \tag{51a}$$

$$\bar{P}_o = (P_o)\left/\left[\frac{M^2\delta_s^2\pi}{4}\left(\frac{\epsilon_o}{\mu_o}\right)^{1/2}\right]\right., \tag{51b}$$

$$\phi_o = \exp\left[-\left(\frac{2L\,\tan\,\phi_s}{\delta_s}\right)^2\right]. \tag{51c}$$

The notation $\text{Re}\{\cdot\}$ indicates that the real part of the enclosed term is taken. Examples of fitting Maker fringe data with fringe patterns computed with Eq. (51a) are given further clarification in the discussion surrounding Figs. 7(f) and 7(g). These examples demonstrate that the approach used to represent the overlapping Gaussian pump and SHG beams works well in fitting the fringe patterns over the entire angular range of θ_i, even though our formalism leading up to Eq. (45) is strictly applicable only to infinite plane waves.

A number of cases described by Eq. (51) are illustrated in Figs. 7(a)–7(d). In all of these figures, $2\delta = 70\,\mu\text{m}$, $\lambda_p = 1064\,\text{nm}$, and the temperature was 25 °C. In Fig. 7(a), $0° < \theta_i < 80°$ and $L = 1.002\,\text{mm}$. Figure 7(b) shows the portion of the graph of Fig. 7(a) where $0° < \theta_i < 18°$ and compares the result with and without pump–SHG overlap. Figure 7(c) compares the result

(a)

(b)

(c)

(d)
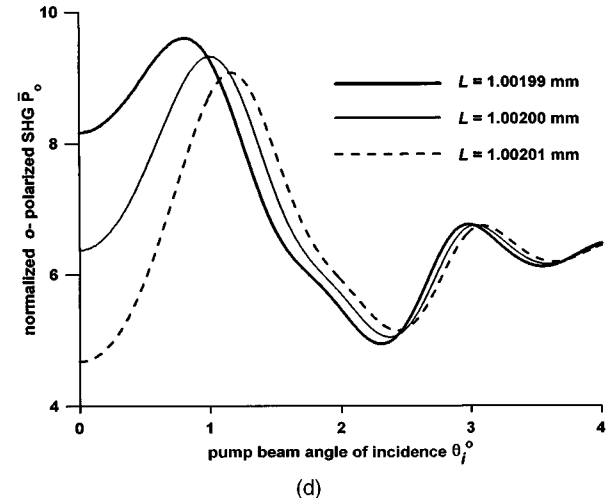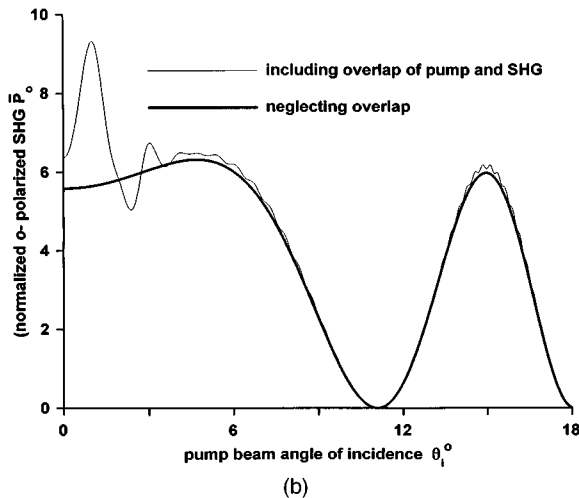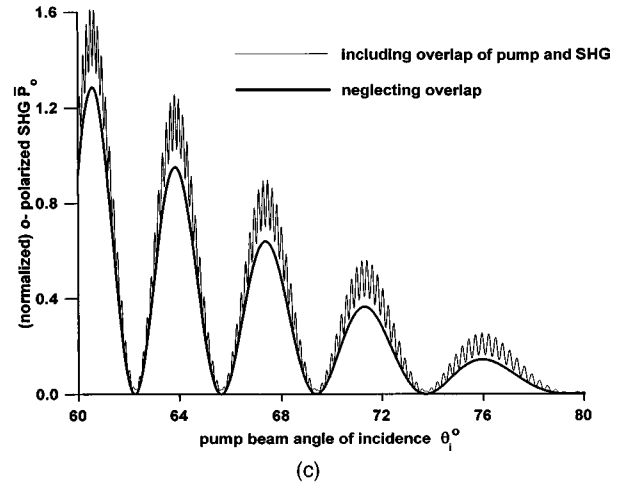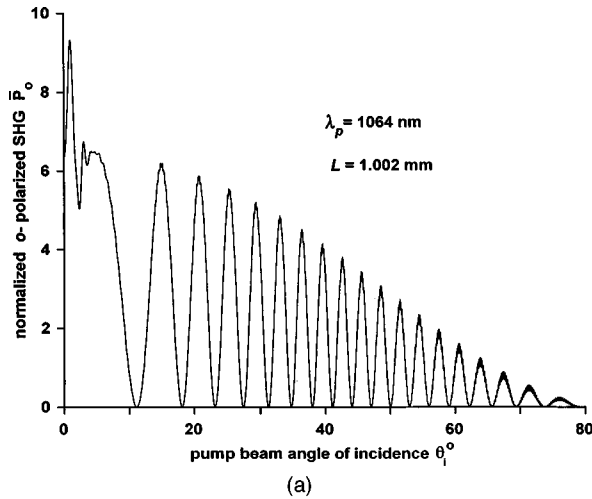
Fig. 7.   Continued on facing page.

with and without pump–SHG overlap over the portion of Fig. 7(a) where $60° < \theta_i < 80°$. Figure 7(c) illustrates that the scalar contribution of the internally-reflected o-polarized SHG fields is more pronounced for wider angles of incidence where $E_y^{(T_2)_o}$ and $E_y^{(T_4)_o}$ do not overlap and interfere. As shown above in Fig. 5(b), where the pump–SHG overlap was neglected, the o-polarized Maker fringe patterns allow the resolution of sample thickness variations with a precision of approximately ± 0.1 μm. Figure 7(d) illustrates that the inclusion of the pump and SHG overlap increases this precision to approximately ± 0.01 μm for $0° < \theta_i < 2°$.

To a first approximation, an o-polarized Maker fringe

pattern generated for a thickness L is equivalent to patterns generated with thicknesses $L \pm 2ml_c^o$, where m is an integer and the coherence length l_c^o for the o-polarized SHG interaction is defined by $l_c^o = \lambda/2(n_o - n_o^p)$. Using the Sellmeier equation, we find $l_c^o = 5.846$ μm. This suggests that an inherent degeneracy exists, and attempts to use the Maker fringe analysis to measure absolute sample thickness will be ambiguous by integer multiples of $2l_c^o$. However, the fringe patterns generated with $L = 1$ mm and $L = 1$ mm $\pm 2l_c^o$ are clearly distinguished for $\theta_i > 40°$. Assuming negligible variation in sample thickness over the region of a single Maker fringe scan, this aperiodicity of the o-polarized SHG fringes

(e)

(g)

(f)
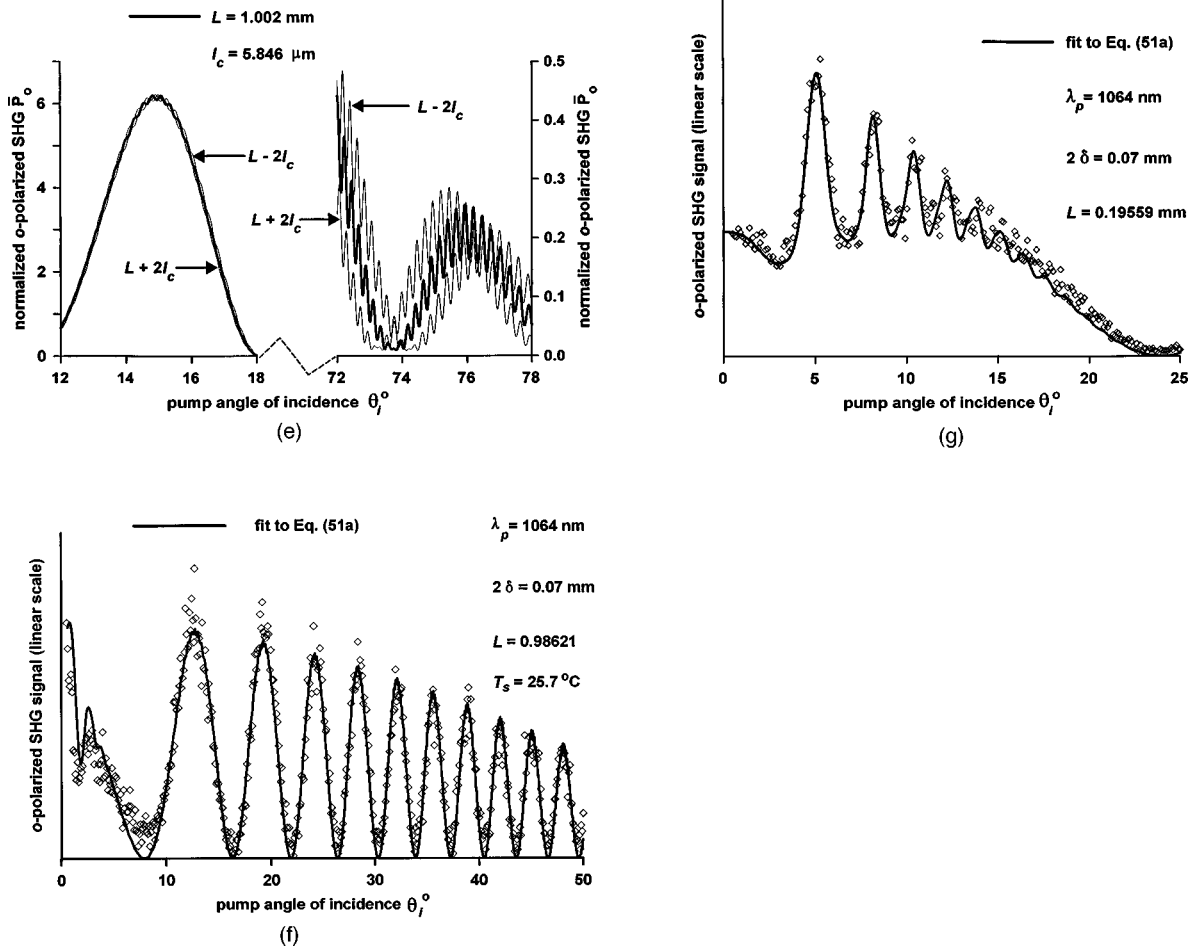
Fig. 7. (a) Normalized o-polarized SHG $\bar{P}_o$ as a function of θ_i that includes the effect of pump and SHG overlap. Note that the influence of multiple-pump reflections is most evident near normal incidence, whereas the effects of multiple SHG reflections are stronger at the extreme range of θ_i. Here $\lambda_p = 1064$ nm, $T_s = 25$ °C, $L = 1$ mm, and $2\delta = 70$ μm. (b) $\bar{P}_o$ (including pump and SHG reflections) compared with $\bar{P}_o^{(T_2)}$ (neglecting such reflections) over the range $0° < \theta_i < 18°$. Here $\lambda_p = 1064$ nm, $T_s = 25$ °C, and $L = 1$ mm. (c) $\bar{P}_o$ (including pump and SHG reflections) compared with $\bar{P}_o^{(T_2)}$ (neglecting such reflections) over the range $60° < \theta_i < 80°$. Here $\lambda_p = 1064$ nm, $T_s = 25$ °C, $L = 1$ mm, and $2\delta = 70$ μm. (d) $\bar{P}_o$ over the range $0° < \theta_i < 4°$ illustrating variations in resolution of thickness where $L = 1$ mm ± 0.01 μm. Over this range of θ_i with $2\delta = 70$ μm, the sensitivity of $\bar{P}_o$ to small changes in thickness is dominated by the multiple reflections of the pump field. Here $\lambda_p = 1064$ nm and $T_s = 25$ °C. (e) Graphs illustrating the approximate periodic nature of $\bar{P}_o$ where $L = 1.002$ mm $\pm 2l_c$, $l_c = 5.846$ μm, $\lambda_p = 1064$, and $T_s = 25$°C. For $0° < \theta_i < 18°$ all three graphs are nearly identical whereas for wider angles, $70° < \theta_i < 90°$, for example, the graphs are clearly distinct and do not overlap. (f) Fitting of Eq. (51a) to an o-polarized Maker fringe pattern that was collected at $T_s = 25.7$ °C. The fit shown was obtained with $L = 0.98621$ mm ± 0.01 μm, $\lambda_p = 1064$, and $2\delta = 70$ μm. (g) Fit of Eq. (51a) to an o-polarized Maker fringe data set is shown for a sample nominally 0.2 mm in thickness. The pump beam was polarized parallel to the y axis, and the sample was a z-cut LiNbO$_3$ plate rotated about the y-axis during the collection of the SHG data. With L varied as the fitting parameter, the result shown illustrates the fit when $L = 0.19559$ mm ± 0.01 μm.

therefore permits fitting the fringe pattern to a unique value of L, provided that θ_i is sufficiently large. For example, with a nominally 1-mm-thick sample an unambiguous coarse estimate of thickness (within ± 0.1 μm) may be obtained first by fitting the o-polarized SHG fringes in the range $5° < \theta_i < 80°$; a fine (within 0.01 μm) estimate of thickness is then obtained by fitting the remaining fringes near normal incidence. The success of fitting thickness to o-polarized SHG data is illustrated in Fig. 7(f). If the range of the data is restricted to $8° < \theta_i < 50°$, the value of L yielding the fit shown is 0.9862 mm ± 0.1 μm. To simultaneously fit the portion of the o-polarized data within the range $0° < \theta_i < 8°$, where the high-frequency fringe oscillations are dominated by the multiple passes of the pump, the precision of L must be increased to 0.98621 mm ± 0.01 μm. The accuracy of this computation method is determined by the uncertainty in n_o, which is believed to be $\pm 2 \times 10^{-4}$. This limitation was mentioned above in conjunction with the temperature-dependent Sellmeier equation of Edwards and Lawrence, which relies heavily on the experimental data of Nelson and Mikulyak.[14,15]

To better illustrate the fit of the model with the o-polarized fringes produced by multiple-beam interference of the pump and SHG, a plate of nominal thickness 0.2 mm was used. The sample for this experiment was a z-cut plate, since a similarly thick x-cut plate was unavailable. For the pump polarization parallel to the y-axis and sample rotation about this axis, otherwise identical x- and z-cut samples will produce the same o-polarized Maker fringe patterns. The resulting o-polarized Maker fringe data are illustrated in Fig. 7(g). The fit of the model to the data yields the superposition shown for a sample thickness of 0.19559 mm ± 0.01 μm. As is discussed in some detail in Section 4, with x-cut plates the o-polarized fringes in the vicinity of normal incidence can often be corrupted by leakage of the more intense e-polarized SHG signal. This effect can occur as a result of the presence of photoelastic strain in the sample. The irregularity of the o-polarized SHG data in the range where $0° < \theta_i < 15°$ for the x-cut sample results that appear in Fig. 7(f) can be attributed to such an effect. Use of a y-pumped z-cut sample rotated about the y-axis permits a clean illustration of the high-frequency fringes near $\theta_i = 0$ without complications of leakage introduced by the e-polarized component. This follows since the corresponding e-polarized SHG signal is necessarily minimal near normal incidence.

B. e-Polarized Maker Fringes Corrected for Multiple Internal Reflections

We now examine the contributions arising from internal reflections of the e-polarized SHG. The e-polarized amplitude component $E_z^{(R_2)_o}$ of the SHG field generated at $x = L$ and propagating toward $x = 0$ is

$$E_z^{(R_2)_o} = E_z^{(T_2)_o} - E_z^o \exp(ik_x^s L) - A_z \exp(ik_x^p L) - A_z^{(2)}. \tag{52}$$

Consider Fig. 3. The fields transmitted and reflected from the surface at $x = 0$, owing to $E_x^{(R_2)}$ and $E_z^{(R_2)}$, are

$$E_x^{(T_3)} = E_x^{(T_3)_o} \exp[i(-k_x x + k_z z - \omega t)], \tag{53a}$$

$$E_z^{(T_3)} = E_z^{(T_3)_o} \exp[i(-k_x x + k_z z - \omega t)], \tag{53b}$$

$$E_x^{(R_3)} = E_x^{(R_3)_o} \exp[i(k_x^s x + k_z^s z - \omega t)], \tag{53c}$$

$$E_z^{(R_3)} = E_z^{(R_3)_o} \exp[i(k_x^s x + k_z^s z - \omega t)], \tag{53d}$$

respectively. We omit factors proportional to $R^4 A_x$ and $R^4 A_z$, since such terms are assumed negligible. The fields reflected and transmitted at $x = L$, owing to $E_x^{(R_3)}$ and $E_z^{(R_3)}$, are

$$E_x^{(T_4)} = E_x^{(T_4)_o} \exp\{i[k_x(x - L) + k_z z - \omega t]\}, \tag{54a}$$

$$E_z^{(T_4)} = E_z^{(T_4)_o} \exp\{i[k_x(x - L) + k_z z - \omega t]\}, \tag{54b}$$

$$E_x^{(R_4)} = E_x^{(R_4)_o} \exp\{i[k_x^s(L - x) + k_z^s z - \omega t]\}, \tag{54c}$$

$$E_z^{(R_4)} = E_z^{(R_4)_o} \exp\{i[k_x^s(L - x) + k_z^s z - \omega t]\}. \tag{54d}$$

Using Eqs. (53) and (54), the associated y-polarized magnetic fields, and the boundary conditions for the tangential fields, we arrive at an expression $E_z^{(T_4)_o}$ for the field amplitude component of the second pass of the e-polarized SHG field emerging from the plate at $x = L$

$$E_z^{(T_4)_o} = P_1 \exp(i3k_x^s L) + P_2 \exp[i(k_x^p + 2k_x^s)L]$$
$$+ P_3 \exp(i2k_x^s L) + P_4 \exp[i(k_x^p + k_x^s)L]. \tag{55}$$

The terms $P_1 – P_4$ in Eq. (55) are given by

$$P_1 = T_4 c_1 (b_1 - 1) E_z^o, \tag{56a}$$

$$P_2 = T_4 c_1 [A_z(b_2 - 1) + b_3 A_x], \tag{56b}$$

$$P_3 = -T_4 c_1 A_z^{(2)}, \tag{56c}$$

$$P_4 = T_4 (c_2 A_z^{(2)} + c_3 A_x^{(2)}), \tag{56d}$$

$$c_1 = \left(\frac{a_1 - a_2}{a_1 + a_2} \right), \tag{56e}$$

$$c_2 = \left(\frac{k_x^p - a_2}{a_1 + a_2} \right), \tag{56f}$$

$$c_3 = \frac{k_z^p}{(a_1 + a_2)}, \tag{56g}$$

$$T_4 = \frac{2a_1}{a_1 + a_2}. \tag{56h}$$

The terms a_1 and a_2 are given in Eq. (30). The e-polarized SHG power leaving the plate at $x = L$, which is corrected for both the second pass of the pump and the SHG, is defined by P_e, where
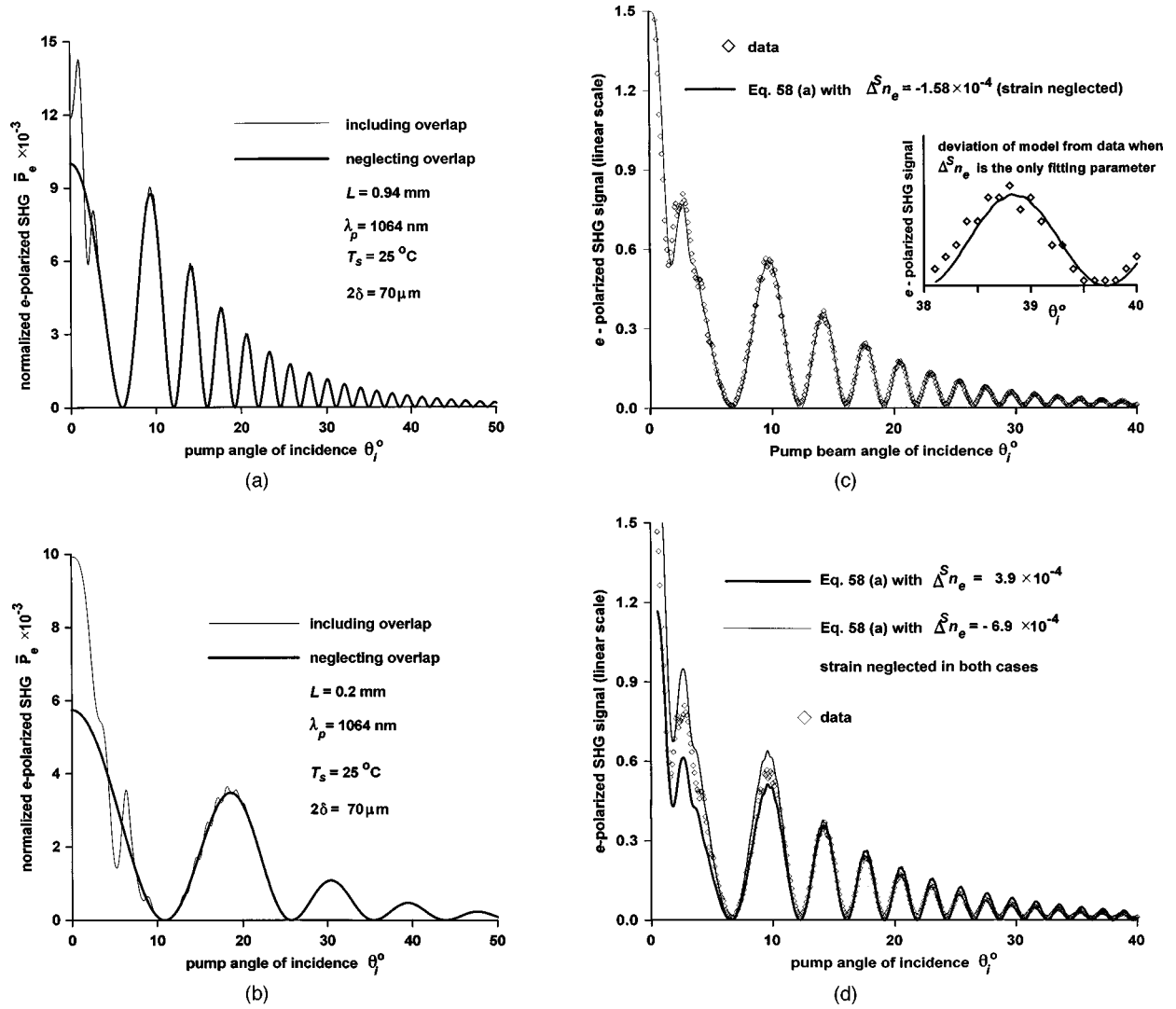
Fig. 8. (a) Comparison of the normalized e-polarized SHG $\bar{P}_e^{(T_2)}$ (neglecting pump and SHG reflections) with the normalized e-polarized SHG $\bar{P}_e$ (including such reflections). Here $\lambda_p = 1064$ nm, $T_s = 25\,°C$, $L = 0.94$ mm, and $2\delta = 70\,\mu$m. (b) Graphs illustrating the same parameters and conditions as Fig. 8(a), except for $L = 0.2$ mm. (c) Fitting Eq. (58a) to an e-polarized Maker fringe pattern that was collected at $T_s = 25.7\,°C$. The value of L computed in regard to Fig. 7(f) was used as an input parameter. With $\Delta^s n_e$ as the only adjustable parameter, the fit shown was obtained with $\Delta^s n_e = -1.58 \times 10^{-4} \pm 5 \times 10^{-6}$, $\lambda_p = 1064$, and $2\delta = 70\,\mu$m. The inset shows the residual deviation of the model from the data for θ_i near 40°. Figure 12(b) shows how the inclusion of strain effects can correct this deviation. (d) Graphs illustrating the approximate periodic nature of Eq. (58a) with respect to shifts in the extraordinary index where $\Delta^s n_e = -1.58 \times 10^{-4} - 5.32 \times 10^{-4}$ and $\Delta^s n_e = -1.58 \times 10^{-4} + 5.48 \times 10^{-4}$. The sample temperature and thickness are the same as used for Fig. 8(c). The two graphs show reasonable overlap with the same e-polarized SHG data set appearing in Fig. 8(c) with regard to locating the fringe nulls. However, neither graph shows an acceptable fit of the fringe envelope in comparison with Fig. 8(c).

$$P_e = \frac{1}{2}\left(\frac{\epsilon_o}{\mu_o}\right)^{1/2}\left\{ \int_0^{2\pi}\int_0^\infty [|E_x^{(T_2)_o}|^2 + |E_x^{(T_4)_o}|^2 + |E_z^{(T_2)_o}|^2\right.$$

$$+ |E_z^{(T_4)_o}|^2]\exp\left(-\frac{2r^2}{\delta_s^2}\right)r\,dr\,d\alpha$$

$$+ 2\,\mathrm{Re}\int_0^{2\pi}\int_0^\infty \{E_x^{(T_2)_o}[E_x^{(T_4)_o}]^* + E_z^{(T_2)_o}[E_z^{(T_4)_o}]^*\}$$

$$\left.\times \exp\left[-\frac{(r^2 + r_1^2)}{\delta_s^2}\right]r\,dr\,d\alpha\right\}. \tag{57}$$

The normalized field amplitude $\bar{E}_z^{(T_4)_o}$ is defined by

$E_z^{(T_4)_o}/N$. The corresponding normalized e-polarized SHG power leaving the plate at $x = L$ is defined by $\bar{P}_e$, where

$$\bar{P}_e = (|\bar{E}_z^{(T_2)_o}|^2 + 2\,\mathrm{Re}\{\bar{E}_z^{(T_2)_o}[\bar{E}_z^{(T_4)_o}]^*\}\phi_e$$

$$+ |\bar{E}_z^{(T_4)_o}|^2)|(\eta)^2|^2\sec^2(\theta_i), \tag{58a}$$

$$= \frac{P_e}{\left[\dfrac{N^2\delta_s^2\pi}{4}\left(\dfrac{\epsilon_o}{\mu_o}\right)^{1/2}\right]}, \tag{58b}$$

$$\phi_e = \exp\left[-\left(\frac{2L \tan \theta_s}{\delta_s}\right)^2\right]. \tag{58c}$$

A graph of Eq. (58a) is shown in Fig. 8(a) for λ_p = 1064 nm, L = 0.94 mm, δ = 35 μm, and T_s = 25 °C. Superimposed on this graph is a graph of Eq. (31), which neglects the effects of multiple pump and SHG passes. Figure 8(b) illustrates a graph of Eq. (58a), where L = 0.2 mm and the remaining parameters are the same as in Fig. 8(a).

We now consider issues involved in fitting the model to the e-polarized Maker fringe data. The results of Bergman show that a variation in the Li$_2$O composition of 0.3 mol. % leads to an approximate variation in n_e of −0.02 and that the variation in n_o over the same compositional range is negligible.[2] These estimates relating compositional uniformity to birefringence variations are consistent with modern production-quality LiNbO$_3$ crystals, which are reported to have a uniformity of $\pm 5 \times 10^{-3}$ mol. % Li$_2$O and a corresponding variation in birefringence of $\pm 7 \times 10^{-5}$. These data were given in a recent list of specifications provided by a current manufacturer of LiNbO$_3$ (Ref. 21). If we assume that variations in composition are the most significant factors influencing the optical properties of the material, then we may reasonably expect that n_o is well represented by the temperature-dependent Sellmeier equation, whereas compositional variations across a wafer may be revealed by corresponding variations in n_e within the range of $\pm 7 \times 10^{-5}$. Thus the thickness data computed by fitting the model to o-polarized Maker fringe data may be used as input in fitting the corresponding e-polarized data where n_e is used as the fitting parameter. In this fashion, as illustrated in our earlier preliminary work, we produced maps that illustrate the variation of birefringence factor $n_o^p - n_e$ across sample wafers.[3]

Equation (58a) is an approximately periodic function of $n(\theta_s)$ with period $\pm m\lambda/L$, where m is an integer. This is also revealed by inspection of Eq. (31). For a plate of 1-mm nominal thickness $\lambda/L = 5.32 \times 10^{-4}$. Therefore, when the e-polarized Maker fringe data is fit to the model with n_e as a fitting parameter, there is the possibility of ambiguous solutions with n_e centered about multiples of $\pm\lambda/L$. Recall from Subsection 3.A that a similar problem arose in regards to fitting the o-polarized SHG data by variation of the thickness. Figure 8(c) illustrates fitting Eq. (58a) to e-polarized Maker fringe data with the value of L that was computed from the corresponding o-polarized data shown above in Fig. 7(f). During the collection of both e- and o-polarized data, the sample temperature T_s was 25.7 °C. To obtain the fit shown in Fig. 8(c), the deviation of n_e from the Sellmeier value n_e^s was $\Delta^s n_e = -1.58 \times 10^{-4} \pm 5 \times 10^{-6}$ where, from our previous definition, $\Delta^s n_e = n_e - n_e^s$. Figure 8(d) illustrates fitting the model to the same data where n_e was first offset from n_e^s by $\pm\lambda/L$ and then varied to obtain the fits to the data shown. In this case the resulting values of $\Delta^s n_e$ that permitted fitting the data to the theory were 3.90 $\times 10^{-4}$ and -6.90×10^{-4}, respectively. Note that both of these results are in close agreement with −1.58 $\times 10^{-4} \pm \lambda/L$, which yields 3.74×10^{-4} and -6.90×10^{-4}, respectively.

Comparison of Figs. 8(c) and 8(d) reveals that all three fits accurately locate the fringe nulls; however, only Fig. 8(c) simultaneously fits the envelope and the nulls, and we therefore regard the value of $-1.58 \times 10^{-4} \pm 5 \times 10^{-6}$ as correctly representing the deviation of n_e from the Sellmeier equation under the assumption that n_o^p derived from the Sellmeier equation is accurate. The manufacturer's specifications give uncertainties in n_o and n_e (at a wavelength of 632.8 nm) of approximately $\pm 2 \times 10^{-4}$. Thus the uncertainty in n_o^p is roughly a factor of 2.7 less than the index ambiguity introduced by λ/L as illustrated in Figs. 8(c) and 8(d). The conclusion that $\Delta^s n_e$ should be negative and fall in the range of a few parts in 10^{-4} is further discussed in Section 5. Finally, as illustrated with the inset in Fig. 8(c), a closer inspection of the results reveals that as θ_i increases from 20° to 40° a deviation of approximately 0.2° between the predicted and measured positions of the fringe nulls is accumulated. This discrepancy cannot be compensated for by further variation of n_e without degrading the portion of the fit between normal incidence and 20°. In Section 4 we show how the inclusion of photoelastic strain effects may be used to account for this remaining discrepancy.

4. VARIATIONS IN THE MAKER FRINGE PATTERNS THAT ARE DUE TO PHOTOELASTIC EFFECTS

Under the same o-polarized pumping conditions, the intensity of the e-polarized Maker fringes is approximately 10^3–10^4 larger than the corresponding o-polarized fringes. In collecting the o-polarized SHG data we must therefore carefully null the dominant e-polarized signal with a suitable-quality polarizer. Often, however, significant leakage of the e-polarized SHG signal will corrupt the o-polarized fringes, regardless of the care taken to align the sample or the polarizer. A minor example of this effect is present in the data shown in Fig. 7(f), particularly for $0° < \theta_i < 20°$. A severe example of this leakage effect is illustrated in Fig. 9, which shows a superposition of both the e- and o-polarized fringes taken at the same point on the sample. Extra fringes occur in the o-polarized data, which align exactly with the corresponding e-polarized fringes. With the analyzer orientation fixed, this leakage effect may vary drastically for Maker fringe scans taken at positions on the sample separated by less than 1 mm. These effects are routinely seen in many wafers and occur without the presence of scratches, cracks, or obvious flaws. We now consider the role of photoelastic effects in causing these artifacts.[22]

The optical impermeability tensor η_{ij} is defined by $\epsilon_{im} \eta_{ij} = \delta_{mj}$ (where δ_{ij} is the Kronecker delta and should not be confused with our earlier definition of the pump-beam diameter). Variations in η_{ij} that are due to strain are given by the contraction of the photoelastic tensor P_{ijkl} with the strain tensor S_{kl} where

$$\Delta \eta_{ij} = P_{ijkl} S_{kl}. \tag{59}$$

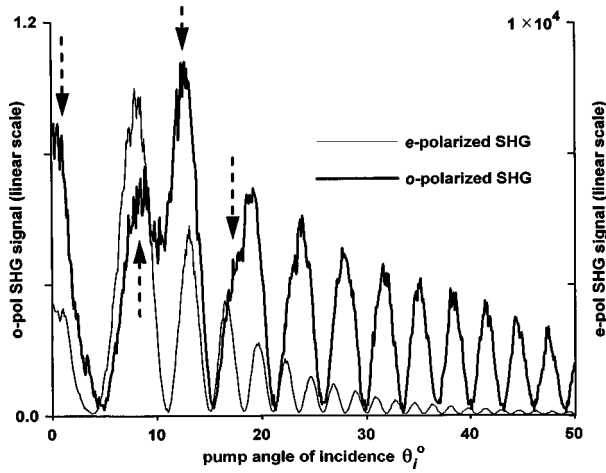The components of the variations to the impermeability tensor are denoted by $\Delta \eta_{ij}$ and reduce to

Fig. 9. Data showing the corruption of the weaker o-polarized Maker fringe data by the dominant e-polarized SHG signal. Note that the extra fringes in the o-polarized data align exactly with the corresponding e-polarized data taken at the same point on the sample as indicated by the arrows. This effect is often highly localized such that an o-polarized scan performed at a position less than 1 mm away may show substantially greater or lesser corruption.

$$\Delta \eta_{11} = P_{11}S_1 + P_{12}S_2 + P_{13}S_3 + 2P_{14}S_4, \quad (60a)$$

$$\Delta \eta_{12} = 2P_{14}S_1 + (P_{11} - P_{12})S_6, \quad (60b)$$

$$\Delta \eta_{13} = 2P_{44}S_5 + 2P_{41}S_6, \quad (60c)$$

$$\Delta \eta_{22} = P_{12}S_1 + P_{11}S_2 + P_{13}S_3 - 2P_{14}S_4, \quad (60d)$$

$$\Delta \eta_{23} = P_{41}S_1 - P_{41}S_2 + 2P_{44}S_4, \quad (60e)$$

$$\Delta \eta_{33} = P_{31}S_1 + P_{31}S_2 + P_{33}S_3. \quad (60f)$$

In Eq. (60), $\Delta \eta_{ij} = \Delta \eta_{ji}$ for $i \neq j$. Variations in the dielectric tensor $\Delta \epsilon_{ij}$ that are due to variations in the impermeability tensor $\Delta \eta_{ij}$ follow from differentiation of $\epsilon_{im} \eta_{mj} = \delta_{ij}$, where

$$\Delta \epsilon_{ij} = -\epsilon_{im} \Delta \eta_{mn} \epsilon_{nj}. \quad (61)$$

The components of $\Delta \epsilon_{ij}$ are

$$\Delta \epsilon_{11} = -(\epsilon_{11})^2 \Delta \eta_{11}, \quad (62a)$$

$$\Delta \epsilon_{12} = -\epsilon_{11}\epsilon_{22} \Delta \eta_{12}, \quad (62b)$$

$$\Delta \epsilon_{13} = -\epsilon_{11}\epsilon_{33} \Delta \eta_{13}, \quad (62c)$$

$$\Delta \epsilon_{22} = -(\epsilon_{22})^2 \Delta \eta_{22}, \quad (62d)$$

$$\Delta \epsilon_{23} = -\epsilon_{22}\epsilon_{33} \Delta \eta_{23}, \quad (62e)$$

$$\Delta \epsilon_{33} = -(\epsilon_{33})^2 \Delta \eta_{33}. \quad (62f)$$

The tensor $\Delta \epsilon_{ij}$ is symmetric: $\Delta \epsilon_{ij} = \Delta \epsilon_{ji}$ for $i \neq j$.

Consider that the leakage of the e-polarized SHG into the o-polarized SHG is caused by a strain-induced rotation of the optic axis about the x axis by an angle ζ. The situation is illustrated in Fig. 10. The unprimed coordinate system represents the geometric axes of the crystal, which also conforms to the transmission axis of the output polarizer. The sample is rotated about the y axis during the recording of the Maker fringe data. In the presence of a strain or a collection of strains, which couple y and z, the unprimed axes are no longer the principal

axes of the crystal and the dielectric tensor ϵ_{ij} is not diagonal. The primed axes y' and z' represent the new coordinate system where the dielectric tensor ϵ'_{ij} is diagonal. The fully rigorous approach is to transform d_{ijk} into the new coordinate system and thus find the terms d'_{22} and d'_{31} and the new ordinary and extraordinary indices of refraction. Experimentally, however, the actual angle ζ is typically a few milliradians; thus we work within the approximation that $d'_{31} = d_{31}$ and $d'_{22} = d_{22}$. The additional o'-polarized SHG field arising from this leakage effect is the projection of the e'-polarized component $\bar{E}_z^{(T_2)'}_o$ onto the original y axis as defined by the output polarizer. Within our approximation $\bar{E}_z^{(T_2)'}_o \sim \bar{E}_z^{(T_2)}$. For simplicity, we consider this effect only within the single-pass approximation of the pump and SHG fields.

We now estimate the strain-induced rotation of the optic axis based on the SHG leakage. A collection of strains that result only in the rotation of the optic axis about the x-axis modifies the dielectric tensor and introduces the off-diagonal term ξ, where

$$\epsilon_{ij} = \begin{bmatrix} n_o^2 & 0 & 0 \\ 0 & n_o^2 & \xi \\ 0 & \xi & n_e^2 \end{bmatrix}. \quad (63)$$

From Eq. (62e), the photoelastic strain factor ξ is given by

$$\xi = -(n_e n_o)^2 [P_{41}(S_1 - S_2) + 2P_{44}S_4]. \quad (64)$$

S_1 and S_2 are both axial strains, and S_4 is a shear strain. The dielectric tensor ϵ_{ij} may be transformed into a new system of coordinates in which it is diagonal by application of a_{ki}, where

$$\epsilon'_{kl} = a_{ki}a_{lj}\epsilon_{ij}, \quad (65a)$$

$$a_{ki} = \begin{bmatrix} 1 & 0 & 0 \\ 0 & \cos \zeta & \sin \zeta \\ 0 & -\sin \zeta & \cos \zeta \end{bmatrix}. \quad (65b)$$

The nonzero terms of ϵ'_{ij} are

$$\epsilon'_{11} = \epsilon_{11}, \quad (66a)$$

$$\epsilon'_{22} = \epsilon_{22} \cos^2 \zeta + \epsilon_{33} \sin^2 \zeta + \xi \sin 2\zeta, \quad (66b)$$

$$\epsilon'_{23} = [\epsilon_{33} - \epsilon_{22}] \frac{\sin 2\zeta}{2} + \xi \cos 2\zeta, \quad (66c)$$

$$\epsilon'_{33} = \epsilon_{22} \sin^2 \zeta + \epsilon_{33} \cos^2 \zeta - \xi \sin 2\zeta. \quad (66d)$$

The transformed tensor ϵ'_{ij} is diagonal if $\epsilon'_{23} = 0$. The angle of rotation ζ that makes ϵ'_{ij} diagonal reduces to the approximate expression

$$\zeta \sim \frac{\xi}{(\epsilon_{22} - \epsilon_{33})}. \quad (67)$$

The resulting y-polarized SHG field emerging from the plate at $x = L$, which includes the contribution that is due to the leakage of the z-polarized component, is $E_y^{(T_2)_o} + \zeta E_z^{(T_2)_o}$. To properly scale the leakage artifact as it appears in the Maker fringes, we must weigh the normalized amplitudes $\bar{E}_y^{(T_2)_o}$ and $\bar{E}_z^{(T_2)_o}$, which were com-
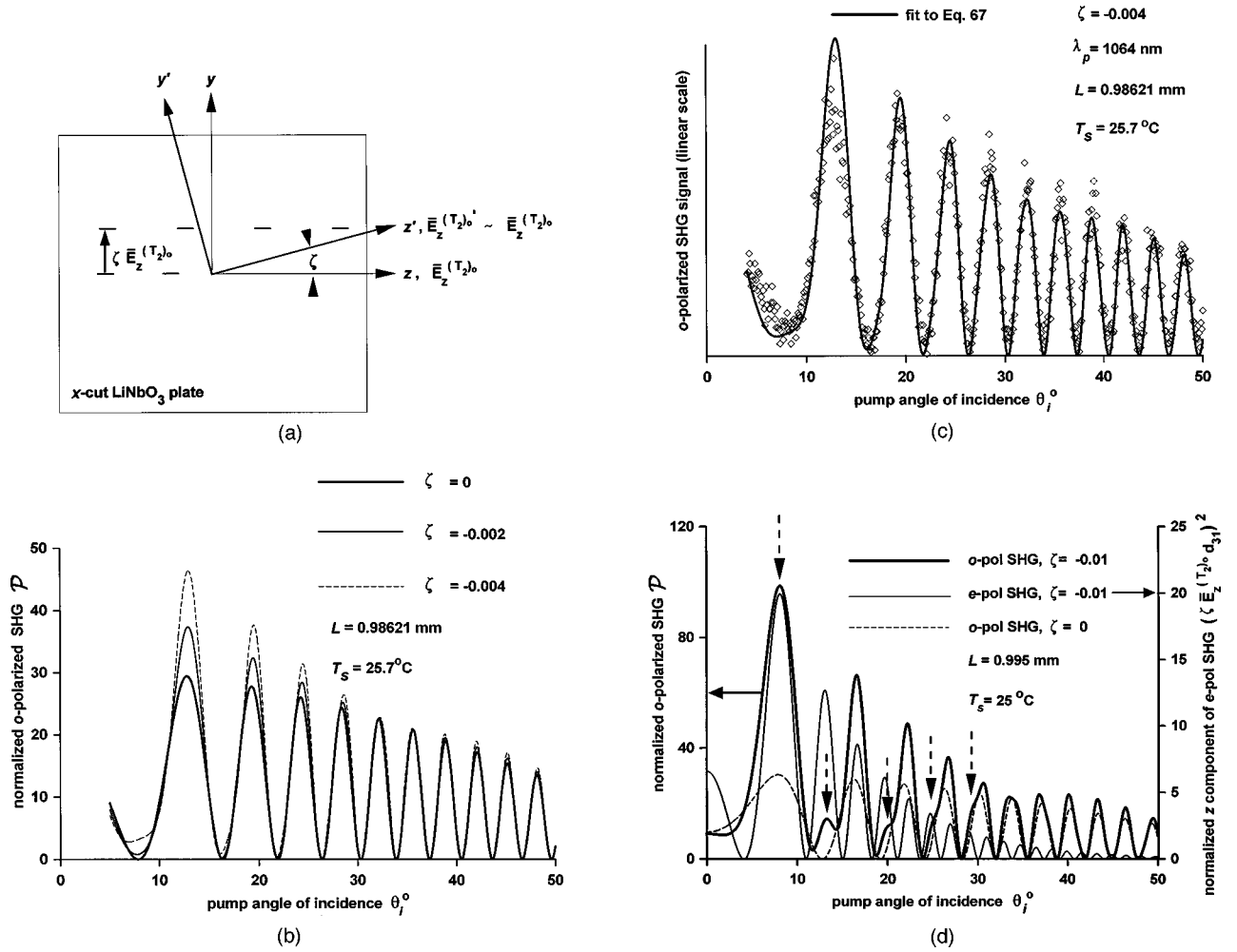
Fig. 10. (a) Schematic of the strain-induced rotation of the optic axis about x by an angle ζ, leading to leakage of the e-polarized SHG signal into the o-polarized data as shown in Fig. 9. The transformed axis z' is associated with the transformed extraordinary index n_e' and the transformed normalized e'-polarized SHG field $\bar{E}_z^{(T_2)'}$. The transformed axis y' is associated with the transformed ordinary indices $n_y^{p'}$ and n_y' at the pump and SHG wavelengths, respectively. The y axis conforms with the orientation of the output polarizer used to separate the e- and o-polarized SHG signals. The projection of $\bar{E}_z^{(T_2)'}$ onto y is approximately $\zeta\bar{E}_z^{(T_2)}$. (b) Normalized o-polarized SHG $\mathcal{P}$ in the presence of strain-induced leakage of $\zeta\bar{E}_z^{(T_2)}$. The case in which strain-induced rotation of the optic axis $\zeta = 0$ is compared with $\zeta = -0.002$ and $\zeta = -0.004$. (c) Improved fit of the o-polarized SHG data shown above in Fig. 7(f) when a strain induced rotation $\zeta = -0.004$ is included. (d) Appearance of extra features in the o-polarized SHG fringes that conform to the corresponding e-polarized fringes are indicated by the vertical arrows. The angle $\zeta = -0.01$.

puted above, with the respective nonlinear coefficients d_{22} and d_{31}. We now define the normalized y-polarized SHG power $\mathcal{P}_o$ that leaves the plate at $x = L$ as $\mathcal{P}_o = |\bar{E}_y^{(T_2)_o} + \zeta\bar{E}_z^{(T_2)_o}|^2$ or

$$\mathcal{P}_o = |\bar{E}_y^{(T_2)_o}|^2(d_{22})^2 + |\bar{E}_z^{(T_2)_o}|^2(\zeta d_{31})^2$$

$$+ 2\zeta d_{31}d_{22}\,\mathrm{Re}\{\bar{E}_y^{(T_2)_o}[\bar{E}_z^{(T_2)_o}]^*\}. \qquad (68)$$

For purposes of scaling, we define the normalized nonlinear coefficients d_{22} and d_{31}, which are equal to 2.2 and -4.6, respectively. The corresponding nonlinear coefficients d_{22} and d_{31} are equal to 2.2×10^{-12} pm V^{-1} and -4.6×10^{-12} pm V^{-1}, respectively.[23] In Eq. (68) we omitted the multiple passes of the pump and SHG for simplicity. Nevertheless, the expression should be acceptably accurate for $|\theta_i| > 5°$ for the typically 1-mm-thick wafers considered here. For strain-induced rota-

tions of the optic axis about x, the extraordinary SHG component $\bar{E}_x^{(T_2)_o}$ does not contribute to the leakage effect described by Eq. (68). In principle, a rotation of the x-axis about z would be revealed by a strain-induced leakage of the $\bar{E}_x^{(T_2)_o}$ component into $\bar{E}_y^{(T_2)_o}$. However, leakage is most strongly revealed in the majority of cases for $|\theta_i| < 20°$, which suggests that effects that are due to $\bar{E}_z^{(T_2)_o}$ are dominant, since $\bar{E}_z^{(T_2)_o} = -\bar{E}_x^{(T_2)_o}\tan\theta_i$.

Graphical examples of Eq. (68) are given in Fig. 10(b), 10(c), and 10(d). In Fig. 10(b), $T_s = 25.7\,°$C, $L = 0.98621$ mm and three curves are displayed with $\zeta = 0$, $\zeta = -0.002$ rad, and $\zeta = -0.004$ rad, respectively. In Fig. 10(c) the same values of T_s and L are used with $\zeta = -0.004$ rad, and the result is displayed with the experimental data of Fig. 7(f). These graphs are representative of typical data in the sense of displaying a 10–30% deviation of the o-polarized Maker fringe envelopes from

the predicted behavior. From these results we may calculate the approximate magnitude of the strain. Using Eqs. (64) and (67), and the Sellmeier equation evaluated at 25.7 °C, we find

$$\zeta = -66.49[P_{41}(S_1 - S_2) + 2P_{44}S_4]. \qquad (69)$$

Equation (69) does not allow for the unique assignment of the strains responsible for the observed leakage artifacts, nor does it permit separation of the shear strain S_4 from axial strain components S_1 and S_2. It nevertheless permits us to estimate the magnitude of the aggregate strain responsible for the observed leakage artifact. For this approximation we use the values of $P_{41} = -0.151$ and $P_{44} = 0.146$ as given by Avakyants *et al.*[24] Equation (68) then leads to the conclusion that the magnitude of the aggregate strain is $\sim 2 \times 10^{-4}$. In some instances the strain may be substantially higher. Indeed, for the extra e-polarized fringes to be clearly distinguished from the o-fringes, as is the case illustrated in Fig. 9, inspection of Eq. (68) reveals that ζ must be of the order of 0.01 rad. Figure 10(d) illustrates an example of this effect where $T_s = 25$ °C, $L = 1$ mm, and $\zeta = 0.01$ rad.

We now calculate the perturbation to the quantity $n_o^p - n_e$, which is caused by a rotation of the optic axis about x by an angle ζ. From Eqs. (65b) and (66d) we have

$$n_x' = n_o, \qquad (70a)$$

$$n_y^{p'} = n_o^{p'} = [(n_o^p)^2 - (n_e^p\zeta)^2 + 2(\zeta n_o^p)^2]^{1/2}, \quad (70b)$$

$$n_z' = n_e' = [(n_e)^2 - (n_o\zeta)^2 + 2(\zeta n_e)^2]^{1/2}. \qquad (70c)$$

Using $\zeta = 2 \times 10^{-3}$, we find

$$n_o^{p'} - n_e' \sim n_o^p - n_e + 7 \times 10^{-7}, \qquad (71a)$$

$$n_o^{p'} - n_o' \sim n_o^p - n_o - 2 \times 10^{-7}. \qquad (71b)$$

These results indicate that strains that cause the corruption of the o-polarized SHG signal with the e-polarized SHG signal, such that $\zeta \sim 2 \times 10^{-3}$, are not themselves effective in producing separately measurable variations in either the e- or o-polarized fringes by means of direct perturbation of the refractive indices. The minimum variation in $n_o^p - n_e$ that could be resolved from the e-polarized fringes was approximately $\pm 5 \times 10^{-6}$. For the o-polarized fringes, a variation of 2×10^{-7} in the quantity $n_o^p - n_o$ is not resolved when computed with Eq. (51a). However, in the regime of larger strains where $\zeta \sim 10^{-2}$, the direct perturbations to the refractive indices n_e, n_o, and n_o^p are all of the order of 10^{-5}. In this case shifts in the e-polarized fringes that are due to strain are indistinguishable from the effects of compositional fluctuations. Furthermore, the o-polarized fringes would be so heavily corrupted, as illustrated in Figs. 9 and 10(d), that use of such data to compute sample thickness may be problematic.

A feature of the e-polarized SHG that may be attributed to a second photoelastic effect appears as an asymmetric angular displacement of the fringes. The effect is
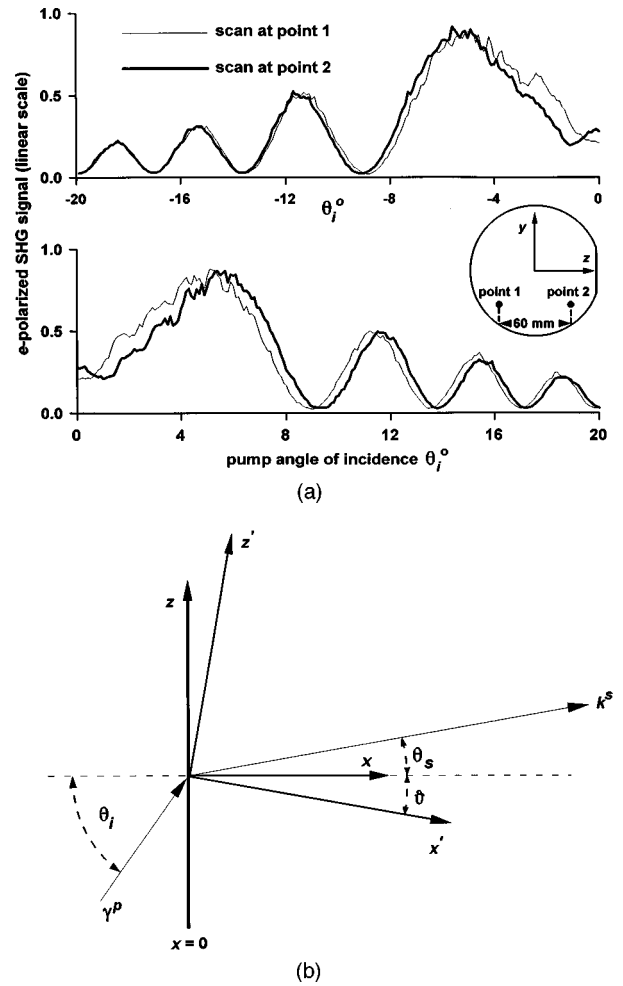

(a)

(b)

Fig. 11. (a) Asymmetric angular shift of e-polarized Maker fringe patterns with respect to pump angle of incidence θ_i. The two e-polarized data scans shown were collected from locations separated by 60 mm on the sample. Note that the relative difference between these data sets is characterized by a symmetric breathing of the fringes with respect to θ_i as well as an asymmetric displacement of the two sets with respect to θ_i. The breathing effect may be described by composition-induced variations in $\Delta^s n_e$, and the asymmetric displacement is described by a strain-induced rotation of the optic axis about y. (b) Schematic illustrating the strain-induced rotation of the optic axis about y by an angle ϑ with respect to the incident pump field, the e-polarized SHG field, and the original crystal axes.

illustrated in Fig. 11(a). This figure shows the superposition of two separate e-polarized Maker fringe scans in which the data were collected consecutively from locations on the sample separated by 60 mm. The rotation stage system was set so that normal incidence of the pump ($\theta_i = 0$) was defined by careful location of the Fresnel reflection of the pump beam folded back into the input optics. A comparison of these two fringe patterns shows a relative displacement with respect to θ_i of approximately 0.1°. Taken together with the results of Subsection 3.B, these results suggest that variations between e-polarized Maker fringes taken at separate positions on a sample can reveal compositional fluctuations through small symmetric fringe displacements and also reveal fluctuations in strain through small asymmetric

fringe displacements. An asymmetric fringe displacement will arise if a strain artifact ψ is present that produces a rotation of the optic axis about y by an angle ϑ. Under such conditions the dielectric tensor becomes

$$\epsilon_{ij} = \begin{bmatrix} n_o^2 & 0 & \psi \\ 0 & n_o^2 & 0 \\ \psi & 0 & n_e^2 \end{bmatrix}. \tag{72}$$

The tensor of Eq. (72) may be put in diagonal form by rotation about y with

$$\epsilon_{kl}' = a_{ki} a_{lj} \epsilon_{ij}, \tag{73a}$$

$$a_{ki} = \begin{bmatrix} \cos\vartheta & 0 & -\sin\vartheta \\ 0 & 1 & 0 \\ \sin\vartheta & 0 & \cos\vartheta \end{bmatrix}. \tag{73b}$$

Performing operations similar to that which resulted in Eq. (67), we find that the angle ϑ that diagonalizes Eq. (72) is approximately given by

$$\vartheta = \frac{\psi}{n_e^2 - n_o^2}, \tag{74a}$$

$$\psi = n_e^2 n_o^2 [P_{44} S_5 + P_{41} S_6]. \tag{74b}$$

This equation shows that shear strains S_5 and S_6 are the only factors that can produce a rotation of the optic axis about y. As a numerical example, let us assume that only the S_6 shear strain is present and that the magnitude of the strain is approximately 1×10^{-4}. We then find that $\vartheta = 1 \times 10^{-3}$ rad or $\sim 0.05°$. The corresponding direct corrections to the indices of refraction assume the same form as Eqs. (70), with

$$n_x' = [n_o^2 - (\vartheta n_e)^2 + 2(\vartheta n_o)^2]^{1/2}, \tag{75a}$$

$$n_y' = n_o, \tag{75b}$$

$$n_z' = [n_e^2 - (\vartheta n_o)^2 + 2(\vartheta n_e)^2]^{1/2}. \tag{75c}$$

Evaluation of Eq. (75c) shows that the direct strain-induced perturbation to the extraordinary index $n_z' - n_e$ is approximately 1×10^{-6} for the strain resulting in $\vartheta = 1 \times 10^{-3}$ rad.

As a consequence of the aggregate effect of S_5 and S_6 shear strains resulting in a net strain of the order of 1×10^{-4}, the greatest perturbation to the quantity $(2\pi/\lambda)L [n_o^p - n(\theta_s)]$ (which defines the principal oscillation period of the e-polarized fringes) is the rotation of the optic axis about y and not the direct strain-induced corrections to n_e or n_o^p. The effect of this rotation on the e-polarized Maker fringe data can then be modeled by reconsidering the boundary conditions on pump and e-

polarized SHG fields at $x = 0$. Figure 11(b) shows that the rotation of the optic axis by ϑ imposes on Eq. (17c) the modification

$$\sin\theta_i = n(\theta_s - \vartheta)\sin\theta_s. \tag{76}$$

With the use of Eq. (10a), Eq. (76) may be solved for $\sin\theta_s$. The result is

$$\sin\theta_s = \left\{ \frac{-(2A_1 A_2 + 4A_3^2 \vartheta^2) + [(2A_1 A_2 + 4A_3^2 \vartheta^2)^2 - 4A_1^2(A_2^2 - 4A_3^2 \vartheta^2)]^{1/2}}{(2A_1^2)} \right\}^{1/2}. \tag{77}$$

Equation (77) was derived under the approximation $\sin\vartheta \sim \vartheta$. The factors A_1, A_2, and A_3 are given by

$$A_1 = (n_e^2 - n_o^2)\sin^2\theta_i - (n_e n_o)^2, \tag{78a}$$

$$A_2 = (n_o \sin^2\theta_i)^2, \tag{78b}$$

$$A_3 = (n_o^2 - n_e^2)\sin^2\theta_i. \tag{78c}$$

Thus θ_s may be written directly as a function of θ_i and ϑ. Equation (77) reduces to Eq. (17c) for $\vartheta = 0$.

As a graphical example of these effects, Fig. 12(a) illustrates the asymmetric shift in the e-polarized fringes that is due to a rotation $\vartheta = -3 \times 10^{-3}$ rad. Superimposed in the figure is a graph where $\Delta^s n_e = 2 \times 10^{-5}$. Comparison of the graphs in Fig. 12(a) reveals that a shift in the e-polarized fringes arising from variations in n_e that are independent of strain may be distinguished from shifts that are due to strain-induced rotations of the optic axis about y. Variations in n_e, which may arise from compositional fluctuations, are revealed by a symmetric breathing of the fringes with respect to θ_i. Strain-induced rotations ϑ are characterized by an asymmetric shift of the fringes. Furthermore, fringe shifts that are due to variations in n_e alone are more evident for $|\theta_i| < 15°$ and become negligible at wider angles, since $n(\theta_s)$ becomes more weighted by n_o. In contrast, the asymmetric fringe shift that is due to ϑ appears nearly uniform over the full range of θ_i. Therefore the different effects of the two perturbation features on the e-polarized Maker fringes allow for the distinction of birefringence variations that arise from strain from those that are due to compositional fluctuations in the material. Figure 12(b) illustrates this feature by displaying an improved fit of the model to the data shown in Fig. 8(c) with the inclusion of a small rotation ϑ. The parameters used to obtain this fit were $\Delta^s n_e = -1.58 \times 10^{-4}$, $L = 0.98621$ mm, $2\delta = 0.07$ mm, just as in Fig. 8(c), and $\vartheta = -8 \times 10^{-4}$ rad. This magnitude of the strain-induced rotation about y corresponds to an aggregate strain that is due to S_5 and S_6 of approximately 8×10^{-5}. In our approach in this section we adopted the simplified view of separately considering rotations ζ and ϑ rather than the more rigorous method of including perturbations ψ and ξ in the dielectric tensor and then finding the rotation angles with a principal axis transformation. Nevertheless, since the angles ζ and ϑ are typically of the order of few milliradians, the simplified approach should remain valid.
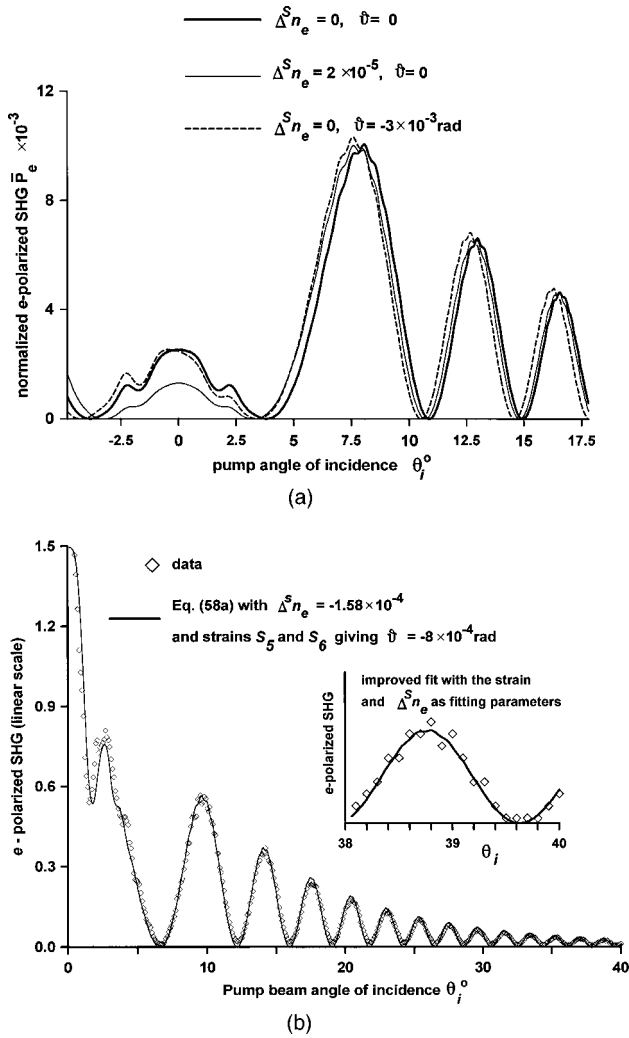
(a)

(b)

Fig. 12. (a) Asymmetric shift in the e-polarized fringes that results with the inclusion of aggregate shear strains that are due to S_5 and S_6, resulting in $\vartheta = -3 \times 10^{-3}$ with $T_s = 25$ °C, $\lambda_p = 1064$, and $2\delta = 70$ μm. Also shown is a graph with $\Delta^s n_e = 2 \times 10^{-5}$. Comparison of these graphs shows that variations in the fringes that are due to $\Delta^s n_e$ are more heavily weighted near normal incidence, whereas while shifts in the fringes that are due to rotations ϑ appear throughout the full range of θ_i. (b) Improvement of the fit shown in Fig. 8(c) by the inclusion of a small strain-induced rotation ϑ of the optic axis about y. $\Delta^s n_e = -1.58 \times 10^{-4}$, $\vartheta = -8 \times 10^{-4}$ rad, $\lambda_p = 1064$, and $2\delta = 70$ μm. The inset details the improved fit for θ_i near 40°.

5. DISCUSSION

The results of Section 4 show that, if the Maker fringe analysis is intended for use in tracking composition gradients across a wafer, we must vary both n_e and ϑ in fitting the model to the e-polarized SHG data. This enables distinguishing birefringence variations that are due to composition from those that are due to strain, provided that the strains are not large enough to produce direct variations in n_e of approximately 10^{-5} or larger. A composition-dependent variation in n_e will produce a symmetric breathing of the fringes, whereas the strains responsible for an optic axis rotation ϑ produce an asymmetric shift in the fringes. The two effects may thus be

distinguished even though the magnitude of the fringe perturbation is approximately the same in either case. This conclusion is further reinforced by the fact that the observed magnitude of the collective strains usually fall in the range of $10^{-5}-10^{-4}$ and are therefore not sufficiently large to cause a directly resolvable increase or decrease in the indices of refraction. Rather, it is the strain-induced *rotations* of the optic axis about x and y that are primarily revealed.

Such a distinction could not be made as easily if the birefringence variation were tracked by means of temperature tuning to produce noncritical phase matching. This point is understood by consideration of Fig. 13. The figure illustrates temperature tuning to achieve noncritical phase matching in an x-cut LiNbO$_3$ sample where $L = 1$ cm. For simplicity, multiple-pump and SHG reflections were ignored and Eq. (31) was used to generate the graphs. The FWHM of both curves shown is ~1.1 °C, and $\Delta^s n_e = -5 \times 10^{-5}$ corresponds to a temperature variation of approximately 1.4 °C. These results show that noncritical phase matching may be used to track birefringence variations with a precision of approximately $\pm 2 \times 10^{-5}$, provided that the sample is ~1 cm in thickness or greater. However, an interaction length of ~1 cm defeats the purpose of crystal uniformity measurements, since such a large volume of material is sampled. Indeed, from a section of boule 1 cm thick it is possible to produce nearly nine finished wafers. By contrast, the Maker fringe analysis method retains a sensitivity to birefringence of approximately $\pm 5 \times 10^{-6}$ for samples in the thickness range of 0.2–1 mm.

The situation illustrated in Fig. 13 predicts a noncritical phase matching temperature T_{pm} of approximately -19.5 °C. This result deviates drastically from T_{pm}, falling in the range of -1.2 °C to -8.5 °C that is expected for modern congruently grown material.[4] In Fig. 14 we show that allowing $\Delta^s n_e$ to vary from -4.8×10^{-4} to -8×10^{-4} will produce graphs of $\bar{P}_e^{(T_2)}$ that enclose this expected excursion of T_{pm}. This observation that $\Delta^s n_e$ must be negative with a magnitude of the order of a few parts in 10^{-4} is consistent with fitting of our model to the data shown in Fig. 8(c). In that case we found $\Delta^s n_e = -1.58 \times 10^{-4}$ at a temperature of 25.7 °C. The fact that these two offsets in n_e do not exactly agree is no
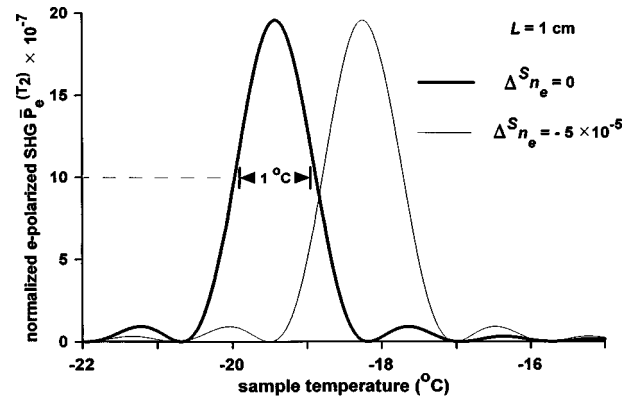

Fig. 13. $\bar{P}_e^{(T_2)}$ as a function of temperature with $L = 1$ cm. The FWHM of $\bar{P}_e^{(T_2)}$ is ~1.2 °C. Also shown is the shift of graph associated with $\Delta^s n_e = -5 \times 10^{-5}$.
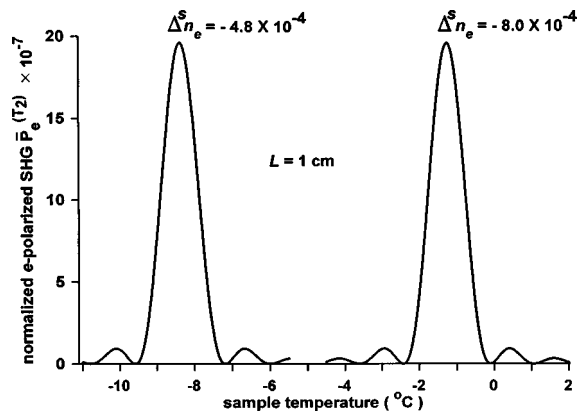
Fig. 14. $\bar{P}_e^{(T_2)}$ is illustrated with $\Delta^s n_e$ varied from -4.8×10^{-4} to -8×10^{-4}. This range of $\Delta^s n_e$ produces graphs of $\bar{P}_e^{(T_2)}$ that bracket the excursion of the phase-matching temperature T_{pm} that is expected for congruently grown material, as discussed in Ref. 4.

cause for concern, since the uncertainty in n_o in the original data that defines the Sellmeier equation is $\pm 2 \times 10^{-4}$. Also, the Sellmeier equation suffers from a systematic error in temperature of 3 °C (see Ref. 14). Since the defining data for the Sellmeier equation was collected at 24.5 °C, we assume that the systematic error in temperature introduces additional uncertainty in the calculated indices of refraction, particularly n_e, for sample temperatures differing substantially from room temperature. Figure 13 may also be used to illustrate that an offset in the Sellmeier equation of 3 °C can be interpreted as $\Delta^s n_e \sim 1 \times 10^{-4}$. Considering all of these uncertainties, the range of $\Delta^s n_e$ predicted with noncritical phase matching for temperatures near 0 °C compares well with the value of $\Delta^s n_e$ calculated in conjunction with the results of Fig. 8(c) for the sample temperature of 25.7 °C.

It is tempting to suggest that measurements of wafer birefringence uniformity may be just as easily evaluated by means of linear optics as by nonlinear optics. Such criticisms, however, are easily dismissed by simple arguments. Consider the sample thickness L. An accurate map or grid of sample thickness is required in order to assess the variation in linear birefringence $n_o - n_e$ over the corresponding positions on the sample. If such a thickness map has been assembled by some means, linear birefringence variations across a sample could be performed by measurement of perturbations in the retardation Φ_L, where $\Phi_L = (2\pi/\lambda_p)(n_o^p - n_e^p)L$. Assuming for the moment that $n_o^p - n_e^p$ is accurately given by the Sellmeier equation and that Φ_L may be measured by conventional methods with an uncertainty of $\pm 0.1°$, for $T = 25$ °C and $L = 1$ mm $\pm$ 3.9 nm, then a variation in birefringence of $\pm 3 \times 10^{-7}$ may be resolved. Thus a thickness uncertainty of ± 3.9 nm would be indistinguishable from birefringence variations within $\pm 3 \times 10^{-7}$. Consequently, birefringence variations of $\pm 3 \times 10^{-6}$ corresponding to excursions in Φ_L of $\pm 1°$ would be clearly distinguishable from thickness variations. By contrast, as shown above in Fig. 4(b), for $\theta_i > 4°$ the e-polarized Maker fringe patterns permit resolving variations in n_e of $\pm 5 \times 10^{-6}$, even with thickness variations of ± 1 μm. The Maker fringe approach therefore offers enormous practical ad-

vantage for resolving variations in birefringence, since the constraint on the thickness resolution is reduced by ~ 3 orders of magnitude. Furthermore, the thickness map derived from the o-polarized SHG data is automatically indexed to the map of birefringence variation derived from the e-polarized data, since both data sets may be collected at the same time. Finally, a thickness-measuring apparatus that is capable of producing nanometer-scale resolution over full-sized LiNbO$_3$ wafers could be constructed. However, the practicality and expense of such a machine is far outweighed by the relative simplicity and economy of the Maker fringe apparatus.

An additional application of the Maker fringe analysis could be for collection of index-of-refraction data over a wide spectral range. The key point is that flat samples could be used, thus eliminating the need to grind precisely shaped prisms that are required for the traditional minimum-deviation method.[15] An outline for the experimental procedure is as follows: Two samples measuring ~ 5 mm^2 are lapped to separate thicknesses, say, 1.0000 and 0.8000 mm. A precision micrometer is used to confirm the thicknesses at the center of the samples. Maker fringe scans are then performed at the same locations. Since the thicknesses are separately known, an iterative fitting procedure applied to the o-polarized Maker fringes would allow the simultaneous solution for both n_o and n_o^p. These data are used to fit the e-polarized fringes, and the associated value of n_e is computed. As a confirmation of the computed value of n_e, the samples are remounted so that they rotate about their z-axes during the collection of the SHG data and the pump is polarized along the z-axis. This scanning orientation will produce e-polarized SHG with the fringe oscillation depending on the quantity $n_e^p - n_e$. Again, since the thicknesses of both test plates are known, an iterative fitting scheme can be used to compute both n_e^p and n_e. A particularly interesting feature of this procedure is that index-of-refraction data at both the pump and SHG wavelengths are directly obtained. A Ti:sapphire laser could serve as a convenient pump source to generate index data in the visible and in the near infrared. A Nd:YAG-pumped OPO could be used to extend the measurement range further into the infrared.

Finally, the observation that shear strains participate strongly in the photoelastic effects that appear as asymmetric displacement of the e-polarized Maker fringes is consistent with the theoretical arguments of Nelson and Lax, who pointed out that rotations play a significant role in the photoelasticity of birefringent crystals in the presence of shear distortions.[24] Furthermore, shear strains in crystalline media are known to be associated with dislocations.[25,26]

6. CONCLUSIONS

Maker fringe analysis is a convenient and powerful tool that may be used for the unambiguous measurements of sample thickness L and birefringence $n_o^p - n_e$, where, for both cases, the accuracy is determined by the accuracy in n_o and n_o^p. Furthermore, the method is sensitive enough to detect variations in birefringence with a resolution of $\pm 5 \times 10^{-6}$ and to distinguish such variations that arise

from composition fluctuations from those that are due to strain, provided that the aggregate strain does not exceed a few parts in 10^{-4}. This sensitivity in birefringence resolution represents an improvement by a factor of ~5 over methods of temperature-tuned noncritical phase matching. Additionally, the thickness resolution scale over which the birefringence is probed is limited by the coherence length of the interaction. Therefore the Maker fringe analysis offers birefringence resolution of $\pm 5 \times 10^{-6}$ in a thickness resolution scale of a few hundred micrometers. The noncritical phase-matching method requires a sample 1–2 cm in thickness to attain a birefringence resolution of approximately $\pm 2 \times 10^{-5}$.

Two distinct effects of strain were apparent in the Maker fringe data: The first was revealed by the leakage of the dominant e-polarized SHG signal into the weaker o-polarized signal. This effect was attributed to an inde-

terminant combination of axial strains S_1 and S_2 and shear strain S_4. The second strain artifact was revealed by an asymmetric shift of the e-polarized Maker fringes with respect to the angle of incidence of the pump beam and was attributed to an indeterminant combination of shear strains S_5 and S_6. For both types of strain phenomenon, the magnitude of the collective strains was typically of the order of a few parts in 10^{-4}. Occasionally, however, larger strains were revealed by the severe leakage of e-polarized SHG signal into the o-polarized data. In the next paper of this series we will present the results of fitting our models to Maker fringe data taken in grid patterns over full LiNbO$_3$ wafers, illustrate maps of wafer uniformity in terms of composition and strain, and compare results generated under chopped continuous-wave, Q-switched, and mode-locked Q-switched pumping conditions.

APPENDIX A: DEFINITION OF SYMBOLS

L, T_s	thickness and temperature respectively, of LiNbO$_3$ sample;
λ_p	vacuum wavelength of the pump field;
$\lambda = \lambda_p/2$	vacuum wavelength of second harmonic field;
ω_p	angular frequency of the pump field;
ω	angular frequency of the second-harmonic field;
θ_i	angle of incidence of pump field;
θ_R	angle of reflection of pump field;
θ_P	angle of refraction of the pump field in the LiNbO$_3$;
θ_{pm}	critical phase-matching angle;
θ_s	angle of refraction of the e-polarized SHG field in the LiNbO$_3$;
ϕ_s	angle of refraction of the o-polarized SHG field in the LiNbO$_3$;
n_o^p	ordinary index at λ_p calculated from the Sellmeier equation of Ref. 14;
n_e^p	extraordinary index at λ_p calculated from the Sellmeier equation of Ref. 14;
n_o	ordinary index at the λ calculated from the Sellmeier equation of Ref. 14;
n_e	extraordinary index at λ derived from fitting e-polarized Maker fringe data;
n_e^s	extraordinary index at λ calculated from the Sellmeier equation of Ref. 14;
$\Delta^s n_e$	$\Delta^s n_e = n_e - n_e^s$;
$n(\theta_s)$	extraordinary index as a function of θ_s;
$\gamma^i = 2\pi/\lambda_p$	magnitude of the wave vector of the incident and reflected pump fields;
$\gamma^p = 2\pi n_o^p/\lambda_p$	magnitude of the pump-field wave vector in the LiNbO$_3$;
γ_x^p, y_z^p	$\gamma^p \cos\theta_P$ and $\gamma^p \sin\theta_P$, respectively;
$k, \kappa = 2\pi/\lambda$	vacuum magnitude of the e- and o-polarized SHG wave vectors, respectively;
k_x, k_z and κ_x, κ_z	$k \cos\theta_i$ and $k \sin\theta_i$, respectively;
$2\gamma^p = k^p \equiv n_o^p k$	magnitude of the wave vector for the nonlinear source polarization;
k_x^p, k_z^p	$k^p \cos\theta_P$ and $k^p \sin\theta_P$, respectively;
$\kappa^s = n_o k$	magnitude of the o-polarized SHG wave vector in the LiNbO$_3$;
κ_x^s, κ_z^s	$\kappa^s \cos\phi_S$ and $\kappa^s \sin\phi_S$, respectively;
$k^s = n(\theta_s)k$	magnitude of the e-polarized SHG wave vector in the LiNbO$_3$;
k_x^s, k_z^s	$k^s \cos\theta_S$ and $k^s \sin\theta_S$, respectively;
$E_y^{P,i}$	amplitude of the y-polarized pump field propagating in the $+x$ direction incident on the LiNbO$_3$ sample at $x = 0$;
E_y^{P,T_1}	amplitude of the y-polarized electric field of the pump propagating in the $+x$ direction transmitted through the surface of the LiNbO$_3$ sample at $x = 0$;
T, R	Fresnel transmission and reflection coefficients, respectively, of the pump at the air–LiNbO$_3$ interface;
P_z	component of the nonlinear source polarization parallel to the LiNbO$_3$ z axis that is due to the y-polarized pump field acting on the d_{31} nonlinear coefficient;

P_y	component of the nonlinear source polarization parallel to the LiNbO$_3$ y axis that is due to the y-polarized pump field acting on the d_{22} nonlinear coefficient;
E_x^o, E_y^o, E_z^o	homogeneous solutions for the SHG electric-field amplitudes propagating in the $+x$ direction arising from the first pass of the pump;
$E_x^{(R_1)_o}$, $E_y^{(R_1)_o}$, $E_z^{(R_1)_o}$	Homogeneous solutions for the SHG electric-field amplitudes propagating in the $-x$ direction generated in reflection from $x = 0$;
$\bar{E}_x^{(R_1)_o}$, $\bar{E}_y^{(R_1)_o}$, $\bar{E}_z^{(R_1)_o}$	normalized versions of $E_x^{(R_1)_o}$, $E_y^{(R_1)_o}$, and $E_z^{(R_1)_o}$;
E_x, E_y, E_z	general inhomogeneous solutions for the SHG electric-field amplitudes propagating through the LiNbO$_3$ in the $+x$ direction arising from the first pass of the pump;
H_x, H_y, H_z	general inhomogeneous solutions for the SHG magnetic-field amplitudes propagating through the LiNbO$_3$ in the $+x$ direction arising from the first pass of the pump;
$E_x^{(R_2)_o}$, $E_y^{(R_2)_o}$, $E_z^{(R_2)_o}$	Homogeneous solutions for the SHG electric-field amplitudes propagating in the $-x$ direction generated by the reflection of the pump at $x = L$;
T_o, R_o	Fresnel transmission and reflection coefficients for $E_y^{(R_2)_o}$ at the LiNbO$_3$–air boundary;
$E_x^{(R_2)}$, $E_y^{(R_2)}$, $E_z^{(R_2)}$	general inhomogeneous solutions for the SHG field amplitudes propagating in the $-x$ direction generated by the reflection of the pump at $x = L$;
$E_x^{(T_2)_o}$, $E_y^{(T_2)_o}$, $E_z^{(T_2)_o}$	solutions for the SHG electric-field amplitudes propagating in the $+x$ direction transmitted through the surface at $x = L$, owing to the first pass of the pump;
$\bar{E}_x^{(T_2)_o}$, $\bar{E}_y^{(T_2)_o}$, $\bar{E}_z^{(T_2)_o}$	normalized versions of $E_x^{(T_2)_o}$, $E_y^{(T_2)_o}$, and $E_z^{(T_2)_o}$;
$E_x^{(T_3)_o}$, $E_y^{(T_3)_o}$, $E_z^{(T_3)_o}$	solutions for the SHG electric-field amplitudes propagating in the $-x$ direction transmitted through the surface at $x = 0$, owing to the second pass of the pump;
$E_x^{(T_4)_o}$, $E_y^{(T_4)_o}$, $E_z^{(T_4)_o}$	solutions for the SHG electric-field amplitudes propagating in the $+x$ direction generated by the reflection of the second pass of the pump at $x = 0$ and transmitted through the second surface at $x = L$;
$\bar{E}_x^{(T_4)_o}$, $\bar{E}_y^{(T_4)_o}$, $\bar{E}_z^{(T_4)_o}$	normalized versions of $E_x^{(T_4)_o}$, $E_y^{(T_4)_o}$, and $E_z^{(T_4)_o}$;
$\bar{P}_e^{T_2}$	normalized e-polarized SHG power leaving the crystal at $x = L$, owing to a single pass of the pump and SHG;
$\bar{P}_o^{T_2}$	normalized o-polarized SHG power leaving the crystal at $x = L$, owing to a single pass of the pump and SHG;
$\bar{P}_e$	normalized e-polarized SHG power leaving the crystal at $x = L$, owing to multiple passes of the pump and SHG;
$\bar{P}_o$	normalized o-polarized SHG power leaving the crystal at $x = L$, owing to multiple passes of the pump and SHG;
ξ	photoelastic strain factor producing a rotation of the optic axis about x;
ζ	angle of rotation of optic axis about x arising from strain factor ξ;
$\mathcal{P}_o$	normalized o-polarized SHG leaving the crystal at $x = L$, which is corrupted by a strain-induced e-polarized component. Only a single pass of pump and SHG is considered;
ψ	photoelastic strain factor producing a rotation of the optic axis about y;
ϑ	angle of rotation of optic axis about y arising from strain factor ψ.

REFERENCES AND NOTES

1. J. Jerphagnon and S. K. Kurtz, "Maker fringes: a detailed comparison of theory and experiment for isotropic and uniaxial crystals," J. Appl. Phys. **41**, 1667 (1970).
2. J. G. Bergman, A. Ashkin, A. A. Ballman, J. M. Dziedzic, H. J. Levinstein, and R. G. Smith, "Curie temperature, birefringence, and phase-matching temperature variations in LiNbO$_3$ as a function of melt stoichiometry," Appl. Phys. Lett. **12**, 92 (1968).
3. N. A. Sanford and J. A. Aust, "Maker fringe mapping of LiNbO$_3$ wafers," in *Lasers and Optics for Manufacturing*, Vol. 9 of 1997 OSA Trends in Optics and Photonics Series, Andrew C. Tam, ed. (Optical Society of America, Washington, D.C., 1997), pp. 23–32.
4. P. F. Bordui, R. G. Norwood, C. D. Bird, and G. D. Calvert, "Compositional uniformity in growth and poling of large-diameter lithium niobate crystals," J. Cryst. Growth **113**, 61 (1991).
5. D. H. Jundt, M. M. Fejer, and R. L. Byer, "Optical properties of lithium-rich lithium niobate fabricated by vapor transport equilibration," IEEE J. Quantum Electron. **26**, 135 (1990).
6. S. R. Lunt, G. E. Peterson, R. J. Holmes, and Y. S. Kim, "Maker fringe analysis of lithium niobate integrated optical substrates," in *Integrated Optical Circuit Engineering II*, S. Sriram, ed., Proc. SPIE **578**, 22 (1985).
7. J. A. Aust, B. Steiner, N. A. Sanford, G. Fogarty, B. Yang, A. Roshko, J. Amin, and C. Evans, "examination of domain-reversed layers in z-cut LiNbO$_3$ using Maker fringe analy-

sis, atomic force microscopy, and high-resolution x-ray diffraction imaging," in *Conference on Lasers and Electro-Optics*, Vol. 11 of 1997 OSA Technical Digest Series (Optical Society of America, Washington, D.C., 1997), pp. 485.

8. J. A. Aust, N. A. Sanford, and J. Amin, "Maker fringe analysis of *z*-cut lithium niobate," in *Proceedings of the 10th Annual Meeting of IEEE Lasers and Electro-Optics Society* (IEEE Lasers and Electro-Optics Society, Piscataway, N.J., 1997), pp. 114–115.

9. P. Bordui, Crystal Telchnology, Inc., Palo Alto, Calif. (personal communication, 1997).

10. N. A. Sanford and J. A. Aust, *Properties of Lithium Niobate and other Novel Ferroelectric Materials,* K. K. Wong, ed., EMIS Data Review Series (Institution of Electrical Engineers, London, UK, to be published).

11. A. Yariv and P. Yeh, *Optical Waves in Crystals* (Wiley, New York, 1984).

12. V. G. Dmitriev, G. G. Gurzadyan, and D. H. Nikogosyan, *Handbook of Nonlinear Optical Crystals* (Springer-Verlag, Berlin, 1991).

13. N. Bloembergen and J. Ducuing, "Experimental verification of the optical laws on non-linear reflection," Phys. Lett. **6**, 5 (1963).

14. G. J. Edwards and M. Lawerence, "A temperature-dependent dispersion equation for congruently grown lithium niobate," Opt. Quantum Electron. **16**, 373 (1984).

15. D. F. Nelson and R. M. Mikulyak, "Refractive indices of congruently melting lithium niobate," J. Appl. Phys. **45**, 3688 (1974).

16. N. Bloembergen and P. S. Pershan, "Light waves at the boundary of nonlinear media," Phys. Rev. **128**, 606 (1962).

17. M. L. Bortz and M. M. Fejer, "Measurement of second-order nonlinear susceptibility of proton-exchanged $LiNbO_3$," Opt. Lett. **17**, 704 (1992).

18. I. Shoji, T. Kondo, A. Kitamoto, M. Shirane, and R. Ito, J. Opt. Soc. Am. B **14**, 2268 (1997).

19. J. F. Lam and H. W. Yen, "Dynamics of optical TE to TM mode conversion in $LiNbO_3$ channel waveguides," Appl. Phys. Lett. **45**, 1173 (1984).

20. D. S. Bethune, "Optical harmonic generation and mixing in multilayer media: extension of optical transfer matrix approach to include anisotropic materials," J. Opt. Soc. Am. B **8**, 367 (1991).

21. Product data provided by Crystal Technology Inc, Palo Alto, Calif.

22. R. S. Weis and T. K. Gaylord, "Lithium niobate: summary of physical properties and crystal structure," Appl. Phys. A: Solids Surf. **37**, 191 (1984). See also, J. F. Nye, *Physical Properties of Crystals* (Oxford U. Press, New York, 1995).

23. R. C. Miller and W. A. Nordland, J. Appl. Phys. **42**, 4145 (1971). There is serious disagreement in the literature regarding the magnitudes of the nonlinear optical coefficients for $LiNbO_3$. For example, our estimate of d_{22} is inferred from Miller's Table I for congruent $LiNbO_3$. Miller's data is normalized to d_{36} for potassium dihydrogen phosphate. The magnitudes of d_{36} for potassium dihydrogen phosphate and d_{31} for $LiNbO_3$ were taken from the recent work of Shoji (Ref. 18 above).

24. L. P. Avakyants, D. F. Kiselev, and N. N. Shchitov, "Photoelasticity of $LiNbO_3$," Sov. Phys. Solid State **18**, 899 (1976).

25. D. F. Nelson and M. Lax, "Theory of the photoelastic interaction," Phys. Rev. B **3**, 2778 (1971).

26. F. R. N. Nabarro, ed., *Dislocations in Solids* (Elsevier, Amsterdam, 1979).